第１９回
核燃焼プラズマ
統合コード研究会

19th Burning Plasma Simulation Initiative (BPSI) Meeting

日時：2022 年 1 月 6 日(木)－7 日(金)
場所：オンライン　　および
九州大学筑紫キャンパス応用力学研究所 2 階大会議室

(Ver. 1, 2022 年 2 月 18 日発行)

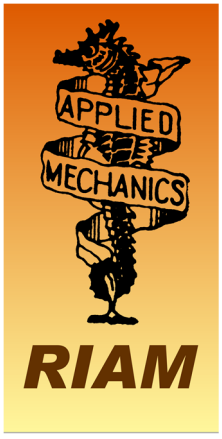

合同会合

第 19 回核燃焼プラズマ統合コード研究会

19th Burning Plasma Simulation Initiative (BPSI) Meeting

および

核融合エネルギーフォーラムサブクラスター会合
シミュレーションクラスター　炉心プラズマモデリングサブクラスター
プラズマ物理クラスター　定常運転・制御サブクラスター

(Ver.1.1)

日時：2022 年 1 月 6 日(木)－7 日(金)
場所：オンライン　および　九州大学筑紫キャンパス　応用力学研究所 2 階大会議室

1 月 6 日(木)

13:00 – 13:10　事務連絡 Business announcement

企画セッション「不純物輸送」 Topical session “Impurity transport”
(座長：矢木)
13:10 – 13:20　講演 1-1　　矢木（量研）
Introduction
13:20 – 13:45　講演 1-2　　相羽（量研）
Current status and issues on developing operation scenarios of fusion DEMO reactor
13:45 – 14:10　講演 1-3　　藤田（名大）
Analysis of impurity transport with TOTAL code in tokamak DEMO
14:10 – 14:30　講演 1-4　　持永（九大）
Impurity transport simulation using integrated code TASK in tokamak plasma
14:30 – 14:40　講演 1-5　　林（量研）
Plan for developing IMPACT: overall plan of the integrated code and its part for impurity transport
14:40 – 14:50　講演 1-6　　本多（京大）
Plan for developing TASK/TX
14:50 – 15:00　議論
Discussion

15:00 – 15:15　休憩

(座長：村上)
15:15 – 15:40　講演 2-1　　Xu (名大)

Reversal of heavy impurity pinch velocity in trapped electron mode turbulence by decreasing the magnetic shear

15:40 – 16:05　講演 2-2　　滝塚（阪大）
Double leap-frog method for large-time-step particle simulation to keep Larmor radius small

16:05 – 16:30　講演 2-3　　本多（京大）
Development of an integrated model GOTRESS+ and its application to assessment of JT-60SA operation scenarios including the pedestal

16:30 – 16:55　講演 2-4　　杉山（量研）
Evaluation of heating power required for L-H transition in JA DEMO

16:55 – 17:20　講演 2-5　　福山（京大）
Progress of wave analyses in toroidal plasmas using the integrated TASK

17:20 – 17:35　休憩

(座長：糟谷)

17:35 – 18:00　講演 2-6　　佐々木（日大）
Study on interaction between micro-turbulence and meso/macro-scale structures based on wave-kinetic formalism

18:00 – 18:20　講演 2-7　　森下（京大）
Development of control system for fusion plasmas using data assimilation

18:20 – 18:35　講演 2-8　　安齋（京大）
Introduction of finite orbital width effects into TASK/FP and comparison with neoclassical transport theory

18:35　散会

1 月 7 日(金)

9:00 – 11:00　ポスター講演 Poster
コアタイム core time　9:00 – 10:00 Group A
10:00 – 11:00 Group B
(開室 start 8:45、閉室 end 13:00)

11:00 – 11:10　休憩

(座長：糟谷)

11:10 – 11:35　講演 3　横山（核融合研）
Information sharing on kick-off meeting of the IAEA-TM on AI application

(Session Leader：村上)

11:35 – 12:00　議論 Discussion

12:00 – 12:10　事務連絡 Business announcement

12:10 – 13:10　昼休み

(核融合エネルギーフォーラムサブクラスターとの合同会合)

13:10 - 13:20　林（量研）
　　サブクラスター関係連絡事項（ITER の統合モデリングエキスパートグループの日本委員交代について）

13:20 - 13:50　宮戸（量研）
　　IFERC 計算機シミュレーションセンターの現状報告

13:50 - 14:20　横山（核融合研）
　　ITER に於ける統合モデリング活動の報告

14:20 – 14:50　若月（量研）
　　ITPA 統合運転シナリオグループ活動報告

14:50 – 15:10　星野（慶應大）
　　炉心プラズマ＋炉工学炉材料モデリングサブクラスター合同会合の報告

15:10 – 15:30　林（量研）
　　今後の予定の議論

15:30　散会

Poster number

19th BPSI meeting (2022.1)

Group A

PA-1 瀬戸春樹（量研) H. Seto

A BOUT++ extension for full annular torus tokamak edge simulations

PA-2 相澤カランザ正臣（日大) M. C. Aizawa

Prediction of turbulence temporal evolution in PANTA by long-short term memory network

PA-3 黒田侑（九大) Y. Kuroda

Analysis of three-dimensional structure of MHD instabilities in tokamak

PA-4 登田慎一郎（核融合研) S. Toda

Prediction of temperature profiles in helical plasmas by integrated code coupled with gyrokinetic transport models

PA-5 糟谷直宏（九大) N. Kasuya

Numerical diagnostic of plasma fluctuations by using 3-D simulation data in torus plasmas

Group B

PB-1 梅崎大介（九大) D. Umezaki

Large-angle scattering transport effects in edge plasma

PB-2 成田絵美（量研) E. Narita

Development of semi-empirical particle and heat transport model and improvement in its turbulent saturation rule

PB-3 髙橋凌一（日大) R. Takahashi

Spatio-temporal analysis of plasma turbulence in PANTA by using singular value decomposition

PB-4 野中奨（九大) S. Nonaka

Effect of impurities on improved confinement in tokamak discharges

PB-5 糟谷直宏（九大) N. Kasuya

Drift wave turbulent structure depending on ion mass number in cylindrical plasmas

Impurity Transport Simulation Using Integrated Code TASK in Tokamak Plasma

S. Mochinaga[1)], N. Kasuya[1,2)], A. Fukuyama[3)], S. Nonaka[1)] and M. Yagi[4)]

[1)] IGES, Kyushu University, [2)] RIAM, Kyushu University, [3)]Kyoto University, [4)]QST

1. Introduction

One of the important issues for realizing a fusion reactor is the control of impurities in the core plasma. In devices that confine high-temperature plasmas, tungsten W can flow into the core from the divertor plates or the first wall, and significantly reduces the plasma performance [1]. Therefore, tungsten control using radio frequency (RF) heating was demonstrated in tokamak plasma experimental devices [2].

In this study, the impurity transport simulation scheme in the integrated code TASK [3] is developed to establish the impurity control scenario using RF heating. In this work, three extensions are made in TASK. Firstly, the transport module is linked to the equilibrium code to include magnetic configuration. Secondly, the scheme is extended to deal with the transport of multiple kinds of impurities such as tungsten, argon, neon, and carbon. Since the impurity transport calculation in TASK has been developed at first focusing on neoclassical transport, the turbulent transport coefficients have been set as given parameters in it. Therefore, thirdly, turbulence models of mixed Bohm/gyro-Bohm model (mBgB) [4] and Multi-Mode-Model (MMM95) [5] are applied. Simulation results with the three extensions is described here.

2. Transport simulation models

The TASK code is one of the integrated codes developed in Japan, which has a modular structure including many codes such as equilibrium, transport, and wave analysis code. The multiple modules exchange data through the data interface BPSD [6], which enables self-consistent simulation.

In the transport calculations of plasma main component using the TASK/TR code, the following particle and heat diffusive one-dimensional transport equations are solved for plasma species s [7].

$$\frac{1}{V'}\frac{\partial}{\partial t}(n_s V') = -\frac{1}{V'}\frac{\partial (V'\Gamma_S)}{\partial \rho} + S_s\,, \tag{1}$$

$$\frac{1}{V'^{5/3}}\frac{\partial}{\partial t}\left(\frac{3}{2}n_s T_s V'^{5/3}\right) = -\frac{1}{V'}\frac{\partial (V' Q_S)}{\partial \rho} + P_s\,, \tag{2}$$

Here, n_s is the plasma density, T_s is the plasma temperature, S_s is the particle source, P_s is the heat source, ρ is the normalized radius, and V' is the radial derivative of plasma volume. The particle flux Γ_s and heat flux Q_s are given as follows;

$$\Gamma_s = \langle|\nabla\rho|\rangle V_s n_s - \langle|\nabla\rho|^2\rangle D_s \frac{\partial n_s}{\partial \rho}\,, \tag{3}$$

and

$$Q_s = \langle|\nabla\rho|\rangle \frac{3}{2} n_s T_s V_{E_s} - \langle|\nabla\rho|^2\rangle n_s \chi_s \frac{\partial T_s}{\partial \rho} + \frac{3}{2}\Gamma_S T_s\,. \tag{4}$$

Here, $<|\nabla\rho|>$, $<|\nabla\rho|^2>$ are the metrics, V_s is the particle convective velocity, D_s is the particle diffusion coefficient, V_{Es} is the heat convective velocity, and χ_s is the heat diffusion coefficient. The diffusion coefficients are given by the sum of neoclassical and turbulent diffusion coefficients, and the convective velocities consist of the neoclassical component only. For the neoclassical transport model, NCLASS [8] is applied. For the transport model of turbulence, mBgB or MMM95 models are applied. The mBgB model can be expressed as follows [9].

$$\chi_e = 8.0\times10^{-5}\chi_B + 3.5\times10^{-2}\chi_{gB}, \tag{5}$$

$$\chi_i = 1.6\times10^{-4}\chi_B + 1.75\times10^{-2}\chi_{gB}, \tag{6}$$

$$D_{e,i} = (0.3+0.7\rho)\frac{\chi_e\chi_i}{\chi_e+\chi_i}\,. \tag{7}$$

The impurity particle diffusion coefficient is $D_Z = D_i$. The Bohm term χ_B and gyro-Bohm term χ_{gB} are given by

$$\chi_B = \rho_s c_s q^2 \frac{a(dp_e/dr)}{p_e}\frac{T_e(\rho=0.8)-T_e(\rho=1.0)}{T_e(\rho=1.0)}, \tag{8}$$

$$\chi_{gB} = \rho_s^2 c_s \frac{(dT_e/dr)}{T_e}\,, \tag{9}$$

where, ρ_s is the gyro radius, c_s is the sound speed and p_e is the electron pressure. The MMM95 model is a theory-based model represented by a linear combination of coefficients by Ion Temperature Gradient (ITG) and Trapped Electron Modes (TEM) of the Weiland model, and Resistive Ballooning (RB) mode and Kinetic Ballooning (KB) mode of Guzdar-Drake model. The diffusion coefficients of MMM95 model are given as follows;

$$\chi_e = 0.80\chi_{e,ITG/TEM} + 1.00\chi_{e,RB} + 1.00\chi_{e,KB}\,, \tag{10}$$

$$\chi_i = 0.80\chi_{i,ITG/TEM} + 0.65\chi_{i,RB} + 1.00\chi_{i,KB}\,, \tag{11}$$

$$D_H = 0.80\chi_{H,ITG/TEM} + 0.65\chi_{H,RB} + 1.00\chi_{H,KB}\,, \tag{12}$$

$$D_Z = 0.80\chi_{Z,ITG/TEM} + 1.00\chi_{Z,RB} + 1.00\chi_{Z,KB}\,. \tag{13}$$

In the impurity transport calculations using the TASK/TI code, the following particle transport equations including atomic processes are solved for k-valent ionized impurity ions.

$$\frac{1}{V'}\frac{\partial}{\partial t}(V'n_k) = -\frac{1}{V'}\frac{\partial}{\partial \rho}(\Gamma_k) + \gamma_{k-1}n_e n_{k-1} - \gamma_k n_e n_k + \alpha_{k+1}n_e n_{k+1}\,, \tag{14}$$

in the case of $k = 1$,

$$\frac{1}{V'}\frac{\partial}{\partial t}(V'n_1) = -\frac{1}{V'}\frac{\partial}{\partial \rho}(\Gamma_1) - \gamma_1 n_1 n_1 + \alpha_2 n_e n_2 - \alpha_1 n_1 - S_0\,, \tag{15}$$

where, γ_k is the ionization rate, α_k is the recombination rate and S_0 is the impurity source. The impurity temperatures are assumed to be equivalent to bulk ion temperature. The γ_k, α_k and radiation loss power of impurity are evaluated with OPEN-ADAS [10] database. In this simulation, the impurity source is set for the 1+ charged impurity ion, assuming that the ions of density n_1 have the thermal velocity v_{th} at the plasma edge. For impurity transport in TASK, the time evolution is solved by linking TR and TI codes. The plasma density and temperature profiles data are transferred from the TR code to the TI code, while the radiation loss power and effective charge number data are transferred from the TI code to the TR code.

3. Impurity transport simulation considering equilibrium

In this section, the effect of introducing an equilibrium in impurity transport is described. In the fixed boundary equilibrium, the major radius $R = 3.0$ m and the minor radius $a = 1.0$ m are kept constant and only the ellipticities are changed from $\kappa = 1.4$ - 1.8. As shown in Fig. 1, the volume derivative increases and the metric $|\nabla\rho|$ decreases with increasing ellipticity.

Assuming that the impurity transport coefficient profiles are constant and the background plasma is given to be fixed as a parabolic profile with the density at the magnetic axis $n_{e0} = 0.5\times10^{19}$m^{-3} and the temperature at the magnetic axis $T_{e0} = T_{i0} = 1.5$ keV, carbon influx from the plasma edge $\Gamma_C = 1.0\times10^{15}$ m^{-2}s^{-1} gives the dependence of the carbon density profiles on the ellipticity in Fig. 2. The impurity density decreases with increasing ellipticity because the decrease in $|\nabla\rho|$ results in a decrease in the effective diffusion. This shows the effect of equilibrium in impurity transport.

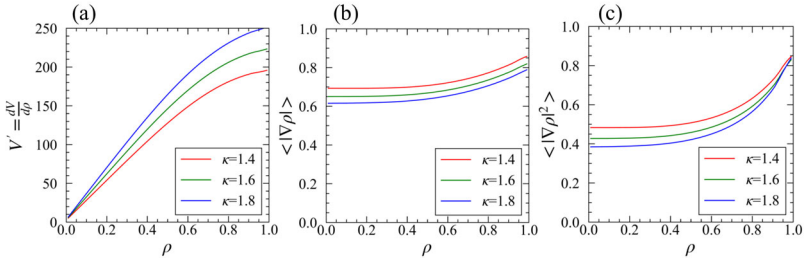

Fig. 1 Radial profiles of (a) the radial derivative of plasma volume, and (b, c) the metric values.

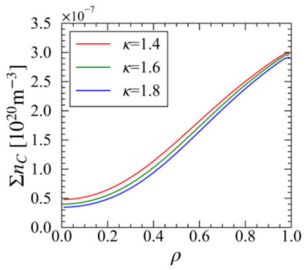

Fig. 2 Ellipticity dependence of carbon density profiles.

4. Transport of multiple impurity species

In this section, simulations for the ITER hybrid scenario [11] with several impurity particle species are described. The plasma parameters of ITER tokamak are $R = 6.0$ m, $a = 2.0$ m, $\kappa = 1.7$, toroidal magnetic field $B_t = 5.3$ T, $I_p = 15$ MA. 30MW of neutral beam (NB) injection and 20MW of ion cyclotron resonance heating (ICRH) are applied as the external heating. The main ion and electron profiles at the steady state for the case when only W, with a concentration of $n_W / n_D = 10^{-6}$, is contained in the plasma are shown in Fig. 3. The plasma density profiles are fixed as in Fig. 3(a). Figure 4 shows the density profiles calculated for Ar only, W only, and both Ar and W cases. The Ar concentration is about 10^{-3} in each case. The turbulent transport coefficients of impurities in these calculations are fixed to be constant in parabola oneas. There is almost no difference in the Ar density profiles, but the W density is smaller in the case including Ar. This is because outward particle pinch of W is slightly larger due to the decrease in the electron temperature caused by the radiation loss of Ar.

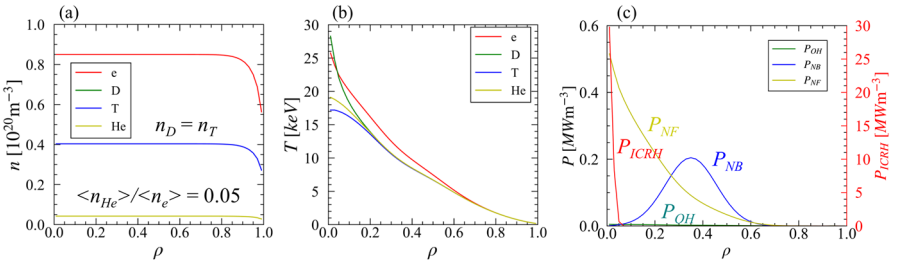

Fig. 3 Radial profiles of (a) plasma density, (b) plasma temperature, and (c) heating power.

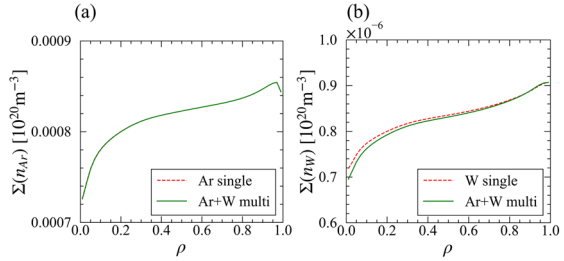

Fig. 4 Radial profiles of (a) Ar and (b) W density. The dashed lines show the density calculated with single impurity species, and the solid lines show the density with multiple impurity species.

5. W transport simulation using turbulence models

In this section, the results of W transport simulations are shown by introducing mBgB and MMM95 models as a turbulent transport model, applied to L-mode plasmas in ASDEX-U tokamak discharges [12]. The plasma parameters are $R = 1.65$ m, $a = 0.5$ m, $\kappa = 1.6$, toroidal magnetic field $B_t = 2.0$ T, $I_p = 0.8$ MA. As shown in Fig. 5, the plasma density and temperature profiles are fixed, referring to the experimental data in Ref. 12. W influx is set to be $\Gamma_W = 5.0\times10^{15}\,\mathrm{m}^{-2}\mathrm{s}^{-1}$.

Figure 6 shows a comparison of the density profiles at steady state using the turbulent diffusion coefficients of the mBgB model, the MMM95 model, and the neoclassical equivalent model that assumes the turbulent diffusion is two times larger than the neoclassical diffusion obtained by NCLASS. The turbulent diffusion coefficients in those cases are shown in Fig. 7. The neoclassical particle pinch component here is inward for $\rho = 0.9$-1.0, and outward up to around $\rho = 0.3$. In the case of the mBgB model, the impurity profile is flattened because the value of the diffusion coefficient is evaluated to be larger in a wider region than the other models. In the case of the neoclassical equivalent model, the value is smaller, so the impurity profile dependents on the pinch component. In the case of the MMM95 model, the Resistive Ballooning mode component is larger near the plasma surface, and the ITG/TEM mode component is larger near the plasma center $\rho < 0.6$. Then, the impurity profile is a little bit hollow.

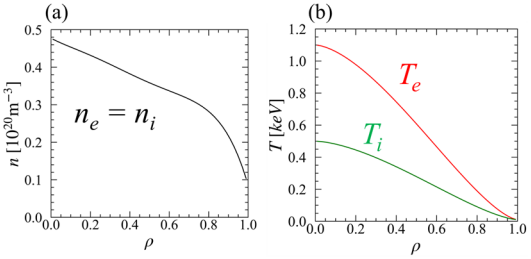

Fig. 5 Radial profiles of plasma (a) density and (b) temperature.

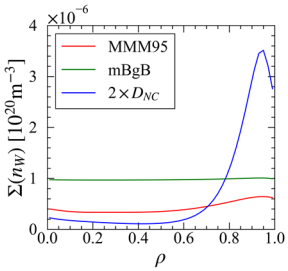

Fig. 6 Radial profiles of W density.

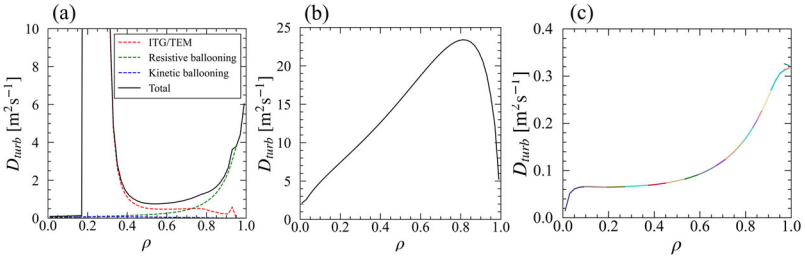

Fig. 7 Radial profiles of the turbulent diffusion coefficients using (a) MMM95 model, (b) mBgB model and (c) the neoclassical equivalent model.

6. Conclusion

Three extensions have been made to the impurity transport simulation scheme in the TASK code: linking transport and equilibrium, enabling the calculation of multiple impurity species, and applying the mBgB and MMM95 models to the impurity turbulent transport model. In the future, the other turbulence model, GLF23 [13], will be applied and impurity control simulation by ECH will be carried out.

References

[1] R. Neu *et al*., Fusion Eng. Des. **65,** 367 (2003).
[2] R. Neu *et al*., Plasma Phys. Control. Fusion **44**, 811 (2002).
[3] M. Honda *et al*., J. Plasma Fusion Res. SERIES **6,** 160 (2004).
[4] M. Erba *et al*., Plasma Phys. Control. Fusion **39**, 261 (1997).
[5] Bateman, Glenn, *et al*., Phys. Plasmas **5**, 1793 (1998).
[6] A. Fukuyama, J. Plasma Fusion Res. **85**, 597 (2009).
[7] S. Mochinaga *et al*., J. Plasma Fusion Res. **16,** 403093 (2021).
[8] W. Houlberg, *et al*., Phys. Plasmas **4**, 3230 (1997).
[9] M. Erba, *et al*., Nuclear Fusion, **38**, 1013 (1998).
[10] ADAS website, http://www.adas.ac.uk/
[11] Na Y.-S. *et al*., J. Korean Phys. Soc. **35** 3788 (2008).
[12] J. Schirmer *et al*. Nuclear Fusion, **46,** 780 (2006).
[13] R. E. Waltz *et al*., Phys. Plasmas **4,** 2482 (1997).

Double Leap-Frog Method for Large-Time-Step Particle Simulation to Keep Larmor Radius Small

T. Takizuka [1], K. Ibano [1], S. Togo [2]

[1] Graduate School of Engineering, Osaka University, Suita 565-0871, Japan
[2] Plasma Research Center, University of Tsukuba, Tsukuba 305-8577, Japan

Modification of the leap-frog (LF) method to keep the Larmor radius ρ small is presented for the particle simulation of a plasma even when $\Omega\Delta t \gg 1$ (Ω: cyclotron frequency, Δt: time step). The conventional LF method makes ρ very large for $\Omega\Delta t \gg 1$, and such a numerical condition has been avoided in general. If the LF method is applicable to the case of $\Omega\Delta t \gg 1$, new particle simulation codes can be more easily developed for a wide area of plasma physics. By repeating the LF steps doubly and adopting the averaged velocity to advance the particle position, the ρ size is kept real independently of the $\Omega\Delta t$ value. Proper nature on the energy conservation, magnetic moment conservation and drift-velocity realization is safely inherited from the LF method.

1. Introduction

Numerical simulation is a powerful tool to understand underlying physics in experimental observations for various fields of plasma science. It is also an indispensable means to predict plasma natures in future experiments, such as fusion reactor etc. Global plasma simulations are especially important for fusion plasma study. MHD/fluid modeling has mainly been applied to them, but it does not sufficiently describe kinetic effects essential for low-collisionality.

Kinetic particle model is then valuable even for global plasma simulations, though it takes a high computational cost. In first-principle particle simulation codes including cyclotron gyration effects, the leap-frog (LF) method has been widely used to integrate equations of motion of an individual numerical particle [1]. The LF method, however, gives a smaller cyclotron frequency $\Omega_{LF} < \Omega = qB/m$, and a larger Larmor radius $\rho_{LF} > \rho = v_\perp/\Omega$ (q: electric charge, m: mass, B: magnetic field, $v_\perp$: speed perpendicular to $\boldsymbol{B}$). Especially in the case of $\Omega\Delta t \gg 1$, Ω_{LF} is limited to $\sim 1/\Delta t \ll \Omega$ and ρ_{LF} is enlarged to $\sim v_\perp \Delta t \gg \rho$ due to the finite time step Δt. Of course particle simulations with gyration motions have generally been carried out under the condition of $\Omega\Delta t \ll 1$. In PARASOL code for edge plasma simulation ($\Omega_e\Delta t \gg 1 > \Omega_i\Delta t$) [2, 3], the ion motion including gyration is solved by the LF method, while the motion of electron guiding center is solved by the predictor-corrector method.

We are studying the ion heat conduction in the mirror field by using PIXY code [4, 5], to find proper formula of the ion heat flux in fluid simulations with anisotropic ion pressure (AIP) model [6, 7]. The PIXY, which treats various kinds of particles to study the plasma-wall interaction, e.g. vapor shielding, is applying only the LF method. This is because the same subroutine can be simply used for motions of multi species. During test simulations of SOL-divertor plasma ($\boldsymbol{B}$ intersects divertor plate obliquely, $B_x/B_t = 1/4$), we surprisingly found that PIXY realized plasma profiles including presheath similar to those simulated by PARASOL, even for $\Omega_e\Delta t \gg 1$ (Fig. 1).

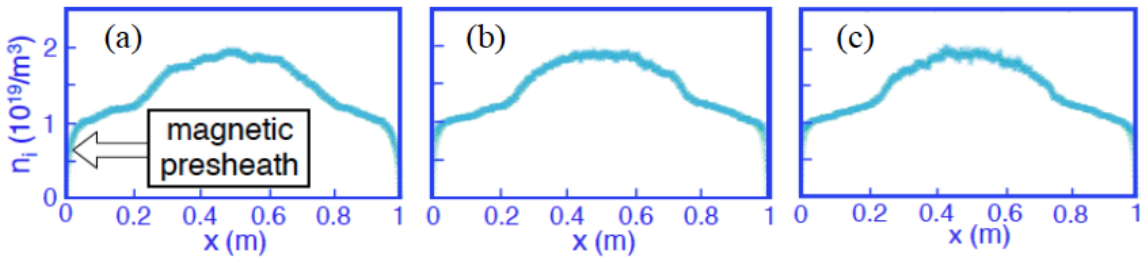

Fig. 1 Density profiles in a SOL-divertor plasma simulated by PIXY for large $\Omega_e\Delta t$ values (a) ~ 6 (B_t = 0.1 T), (b) ~ 30 (B_t = 0.5 T) and (c) ~ 100 (B_t = 2 T). Magnetic presheath was well realized for all cases.

Why does the LF method work well even for very large $\Omega\Delta t$ value? If the LF method is applicable to the large-time-step particle simulation of $\Omega\Delta t \gg 1$, new particle simulation codes can be more easily developed and simulation studies (longer time scale with the larger time step) can be promoted for a wide area of plasma physics. This is our motivation to develop a new algorithm based on the LF method, which is improved to keep the Larmor radius small for large-time-step simulations.

2. Leap-frog method

The LF algorithm for charged-particle motion is written as follows,

$$m\,(\boldsymbol{v}_{+\Delta t/2} - \boldsymbol{v}_{-\Delta t/2})/\Delta t = q\,\{\boldsymbol{E}(\boldsymbol{X}_0) + \tfrac{1}{2}\,(\boldsymbol{v}_{+\Delta t/2} + \boldsymbol{v}_{-\Delta t/2}) \times \boldsymbol{B}(\boldsymbol{X}_0)\} \tag{1}$$

$$(\boldsymbol{X}_{+\Delta t} - \boldsymbol{X}_0)/\Delta t = \boldsymbol{v}_{+\Delta t/2} \tag{2}$$

where the velocity $\boldsymbol{v}$ and position $\boldsymbol{X}$ are set differently from each other with half-time-step separation. The electric field $\boldsymbol{E}$ and magnetic field $\boldsymbol{B}$ in Eq. (1) are chosen at the particle position $\boldsymbol{X}_0$. One of notable merits of the LF method is to assure the energy conservation; $\boldsymbol{v}_+^2 - \boldsymbol{v}_-^2 = (2q\Delta t/m)\,\boldsymbol{E} \cdot \tfrac{1}{2}\,(\boldsymbol{v}_+ + \boldsymbol{v}_-)$.

2.1 Cyclotron frequency and Larmor radius

Considering $\boldsymbol{v}_{\perp,+\Delta t/2} = v_\perp\,(\sin\theta_+, \cos\theta_+, 0)$ with $\theta_+ = \Omega_{\rm LF}\Delta t/2 + \theta_0$ and $\boldsymbol{X}_{\perp,+\Delta t} = \rho_{\rm LF}\,(-\cos\theta, \sin\theta, 0)$ with $\theta = \Omega_{\rm LF}\Delta t + \theta_0$ in a magnetic field $\boldsymbol{B} = (0, 0, B)$, Eqs. (1) and (2) are reduced to

$$\Omega_{\rm LF}\Delta t = 2\tan^{-1}(\Omega\Delta t/2) \tag{3}$$

$$\rho_{\rm LF} = \rho/\cos(\Omega_{\rm LF}\Delta t/2) \tag{4}$$

The simulated cyclotron frequency $\Omega_{\rm LF}$ becomes smaller than real Ω, and the Larmor radius $\rho_{\rm LF}$ is larger than real ρ (see Fig.2). For $\Omega\Delta t < 1$, the relative errors are $\Omega_{\rm LF}/\Omega - 1 = -(\Omega\Delta t)^2/12$ and $\rho_{\rm LF}/\rho - 1 = (\Omega\Delta t)^2/8$. Note that the relation "$\rho_{\rm LF} = v_\perp/\Omega_{\rm LF}$" does not hold. When $\Omega\Delta t \to \infty$, $\Omega_{\rm LF}$ and $\rho_{\rm LF}$ converge to $\pi/\Delta t$ and $v_\perp\Delta t/2$, respectively.

In order to correct the gyro-phase delay, the Boris algorithm has been adopted [8]. Although $\Omega_{\rm Boris}$ is just the real Ω, the Larmor radius is affected as $\rho_{\rm Boris} = \rho\,|(\Omega\Delta t/2)/\sin(\Omega\Delta t/2)|$. When $\Omega\Delta t < 1$, the relative error, $\rho_{\rm Boris}/\rho - 1 = (\Omega\Delta t)^2/24$, is smaller than that of LF method. On the other hand, when $\Omega\Delta t > 1$, the radius is varied bizarrely as seen in Fig. 2 (b); $\rho_{\rm Boris} = v_\perp\Delta t/2$ is similar to $\rho_{\rm LF}$ at $\Omega\Delta t = (2l+1)\pi$, but it becomes infinitely large at $\Omega\Delta t = 2l\pi$ (l: integer).

The enlarged Larmor radius is a fatal demerit of the LF method if applied to $\Omega\Delta t \gg 1$. Strangely, the electron Larmor radius, $\rho_{\rm e,LF} \sim v_{\rm e}\Delta t/2$, becomes larger than that of deuterium ion, $\rho_{\rm i,LF} \sim v_{\rm i}/\Omega_{\rm i}$, when $1 > \Omega_{\rm i}\Delta t > 2v_{\rm i}/v_{\rm e} \sim 1/30$ ($v_{\rm e,i}$:thermal speed of electron and ion) as shown in Fig. 2 (c). Resultantly, the classical diffusion perpendicular to $\boldsymbol{B}$, $D_\perp \approx \rho_{\rm e}^2/\tau_{\rm e}$ ($\tau_{\rm e}$: electron collision time), becomes abnormally larger by $(\Omega_{\rm e}\Delta t)^2$. Reduction of the wave coupling due to $k_\perp\rho_{\rm e,LF} > 1 \gg k_\perp\rho_{\rm e}$ is also the problem.

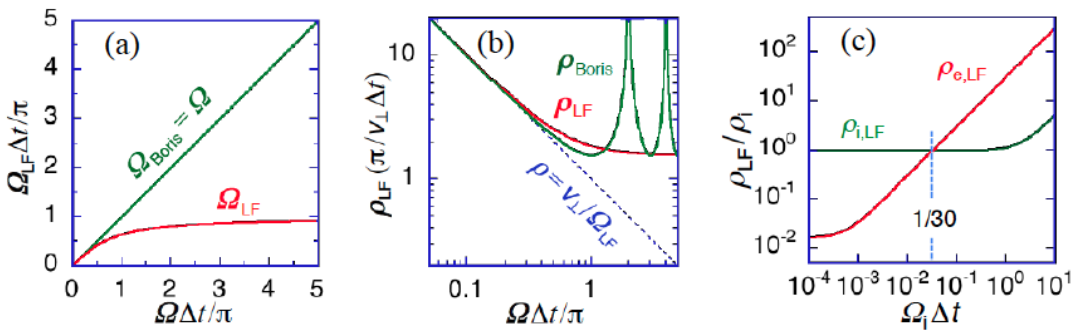

Fig. 2 Time-step dependence of (a) cyclotron frequency and (b) Larmor radius for LF method and Boris algorithm. (c) Electron $\rho_{\rm e,LF}$ becomes larger than ion $\rho_{\rm i,LF}$ when $\Omega_{\rm i}\Delta t > 1/30$ (deuterium ion).

2.2 Magnetic moment and drift

We examine to which extent the LF method correctly simulates the charged particle motion in electric and magnetic fields when $\Omega\Delta t \gg 1$. As described above, $\Omega_{\rm LF}$ and $\rho_{\rm LF}$ converge to $\pi/\Delta t \ll \Omega$ and $v_\perp \Delta t/2 \gg \rho$, respectively. On the other hand, (i) the energy conservation is assured, and (ii) the magnetic moment, $\mu = m v_\perp^2/2B$, is kept constant within the relative error $\sim {\rm O}(\rho_{\rm LF}/L_B)$ or ${\rm O}(1/\Omega_{\rm LF}\tau_B)$. Therefore, (iii) the mirror force parallel to $\boldsymbol{B}$ is realized, $F_{\rm M} = -\mu\nabla_\parallel B$. Here the characteristic length L_B is of the spatial variation of $\boldsymbol{B}$, and the characteristic time τ_B is of its temporal variation. This favorable property is based on a moment $M = m\rho_{\rm LF}|\frac{1}{2}(\boldsymbol{v}_{\perp+} + \boldsymbol{v}_{\perp-})|$ calculated from the r.h.s. of Eq. (1) being fully independent of $\Omega\Delta t$, $M = m\rho_{\rm LF} v_\perp \cos(\Omega_{\rm LF}\Delta t/2) = m\rho_{\rm LF} v_\perp$. As for the drift perpendicular to $\boldsymbol{B}$, (iv) the $\boldsymbol{E}\times\boldsymbol{B}$ drift, $\boldsymbol{V}_{E\times B} = (\boldsymbol{E}\times\boldsymbol{B})/B^2$, is correctly simulated, and (v) the polarization drift, $\boldsymbol{V}_{\rm polar} = ({\rm d}\boldsymbol{E}/{\rm d}t)/B\Omega$, as well. Although $\rho_{\rm LF} \gg \rho$ for $\Omega\Delta t \gg 1$, (vi) the curvature-∇B drift, $\boldsymbol{V}_{\nabla B} = (2v_\parallel^2 + v_\perp^2)(\boldsymbol{B}\times\nabla B)/2B^2\Omega$, can be simulated without worry ($v_\parallel$: speed parallel to $\boldsymbol{B}$).

3. Double leap-frog method

In order to keep the simulated Larmor radius small independently of the $\Omega\Delta t$ value, we propose a new scheme based on the LF method [9]. The usual LF steps are repeated doubly as described below. We call this scheme, therefore, "double leap-frog (DLF)" method.

1st LF step (Virtual position $\boldsymbol{X}'$ and $\boldsymbol{X}^{\#}$)

(i) $\boldsymbol{v}_{+\Delta t/2} - \boldsymbol{v}_{-\Delta t/2} = (q/m)\{\boldsymbol{E}' + \frac{1}{2}(\boldsymbol{v}_{+\Delta t/2} + \boldsymbol{v}_{-\Delta t/2}) \times \boldsymbol{B}'\}\,\Delta t$ (5)

(ii) $\boldsymbol{X}^{\#}_{\Delta t} - \boldsymbol{X}'_0 = \boldsymbol{v}_{+\Delta t/2}\,\Delta t$ (6)

2nd LF step (Tentative velocity $\boldsymbol{v}^{\#}_{+3\Delta t/2}$)

(iii) $\boldsymbol{v}^{\#}_{+3\Delta t/2} - \boldsymbol{v}_{+\Delta t/2} = (q/m)\{\boldsymbol{E}^{\#} + \frac{1}{2}(\boldsymbol{v}^{\#}_{+3\Delta t/2} + \boldsymbol{v}_{+\Delta t/2}) \times \boldsymbol{B}^{\#}\}\,\Delta t$ (7)

(iv) $\boldsymbol{X}_{\Delta t} - \boldsymbol{X}_0 = \boldsymbol{w}_{+\Delta t/2}\,\Delta t$ (8)

averaged velocity $\boldsymbol{w}_{+\Delta t/2} = (\alpha/2)(\boldsymbol{v}^{\#}_{+3\Delta t/2} - \boldsymbol{v}_{-\Delta t/2}) + (1-\alpha)\,\boldsymbol{v}_{+\Delta t/2}$ (9)

with $\alpha = 1/2(1 + \cos(\Omega_{\rm LF}\Delta t/2))$ (10)

Resetting of virtual position

(v) $\boldsymbol{X}'_{\Delta t} - \boldsymbol{X}_{\Delta t} = (\alpha/2)(\boldsymbol{v}_{+\Delta t/2} - \boldsymbol{v}^{\#}_{+3\Delta t/2})\,\Delta t$ (11)

Gyration orbits of $\boldsymbol{X}$ (solid line) and $\boldsymbol{X}'$ (dashed line) are schematically shown in Fig. 3 for $\Omega\Delta t = 2.5$ ($\Omega_{\rm LF}\Delta t = 1.79$ and $\rho_{\rm LF} = 1.60\rho$). The virtual position $\boldsymbol{X}'$ (or $\boldsymbol{X}^{\#}$) moves along an enlarged gyration orbit with $\rho_{\rm LF}$. To keep the real Larmor radius ρ, we use an averaged velocity $\boldsymbol{w}_{+\Delta t/2}$ to advance $\boldsymbol{X}$ in Eq. (8). A simple reduction of the perpendicular movement, $\Delta\boldsymbol{X}_\perp = \boldsymbol{v}_{\perp,+\Delta t/2}\,\Delta t \times \cos(\Omega_{\rm LF}\Delta t/2)$, cannot be applied because the $\boldsymbol{E}\times\boldsymbol{B}$ drift is also reduced. The gyration frequency $\Omega_{\rm LF}$ is not corrected as it is, and the phase relation is the same as that of LF method; $\boldsymbol{X}_\perp \sim \exp(i\Omega_{\rm LF}t)$ and $\boldsymbol{v}_\perp \sim i\exp(i\Omega_{\rm LF}t)$.

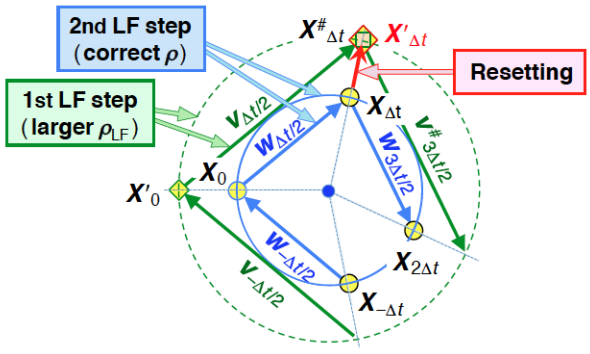

Fig. 3 Gyration orbit of $\boldsymbol{X}$ with correct Larmor radius ρ [2nd step] for $\Omega\Delta t = 2.5$. Velocity $\boldsymbol{v}$, averaged velocity $\boldsymbol{w}$, virtual orbit $\boldsymbol{X}'$ (or $\boldsymbol{X}^{\#}$) with larger $\rho_{\rm LF} = 1.60\rho$ [1st step] and resetting of $\boldsymbol{X}'(\Delta t)$ are schematically shown.

Electric and magnetic fields in Eqs. (5) and (7) are chosen at the virtual position; $\boldsymbol{E}' - \boldsymbol{B}'$ at $\boldsymbol{X}'_0$ and $\boldsymbol{E}^{\#} - \boldsymbol{B}^{\#}$ at $\boldsymbol{X}^{\#}_{\Delta t}$. By this setting, proper nature on the magnetic moment conservation and drift-velocity realization is safely inherited from the LF method. The electrostatic component $\boldsymbol{E}_s = -\nabla\phi$ (ϕ: potential) could be chosen at the real position $\boldsymbol{X}_0$. Since $\boldsymbol{X}_{\Delta t}$ is still not determined before Eq. (7), how to self-consistently treat $\boldsymbol{E}^{\#}$ and $\boldsymbol{B}^{\#}$ is the future problem.

As for the particle flux $\boldsymbol{\Gamma} = n\boldsymbol{U}$ (n: density, $\boldsymbol{U}$: flow velocity), the component parallel to $\boldsymbol{B}$ is calculated at the real position, while the perpendicular flux is calculated at the virtual position to include diamagnetic flow; $\boldsymbol{\Gamma}(\boldsymbol{X}) = \Sigma_j \{S(\boldsymbol{X}-\boldsymbol{X}_j)\, ½\,(\boldsymbol{v}_{\parallel,+\Delta t/2} + \boldsymbol{v}_{\parallel,-\Delta t/2}) + S(\boldsymbol{X}-\boldsymbol{X}'_j)\, ½\,(\boldsymbol{v}_{\perp,+\Delta t/2} + \boldsymbol{v}_{\perp,-\Delta t/2})\}$, where S is a shape function in a Particle-in-Cell simulation (j: particle tag). Note that the diamagnetic flow cannot directly be obtained in the guiding-center system.

The initial value of virtual position $\boldsymbol{X}'(t=0)$ is determined from $\boldsymbol{X}(t=0)$ and $\boldsymbol{v}(t=-\Delta t/2)$ by utilizing the resetting Eq. (11), $\boldsymbol{X}'(0) - \boldsymbol{X}(0) = (\alpha/2)\,\{\boldsymbol{v}(-\Delta t/2) - \boldsymbol{v}^{\#}(\Delta t/2)\}\,\Delta t$, with the tentative-velocity Eq. (7), $\boldsymbol{v}^{\#}(\Delta t/2) - \boldsymbol{v}(-\Delta t/2) = (q/m)\,[\boldsymbol{E}(\boldsymbol{X}(0)) + ½\,\{\boldsymbol{v}^{\#}(\Delta t/2) + \boldsymbol{v}(t-\Delta t/2)\} \times \boldsymbol{B}(\boldsymbol{X}(0))]\,\Delta t$.

Tentative variables $\boldsymbol{X}^{\#}$ and $\boldsymbol{v}^{\#}$ do not continue to the next time-step calculation. Collisional change in $\boldsymbol{v}_{+\Delta t/2}$ then can be given after the above DLF process by using a collision model, such as the Monte-Carlo binary collision model [10].

4. Summary and discussion

Double leap-frog (DLF) method to keep the Larmor radius small is presented for the particle simulation of a plasma even when $\Omega\Delta t \gg 1$ [9]. By repeating the LF steps doubly and adopting the averaged velocity to advance the particle position, the Larmor radius is kept real independently of the $\Omega\Delta t$ value. Proper nature on the energy conservation, magnetic moment conservation and drift-velocity realization is safely inherited from the LF method.

The DLF method for long temporal-scale particle simulation becomes more powerful when coupled with the ingenious model [11,12] for large spatial-scale simulation. The DLF algorithm will be tested during our development of the PIXY code ($\Omega_e\Delta t \gg 1 > \Omega_i\Delta t$) in the near future. The possibility of using this new modeling in kinetic simulations instead of using the gyrokinetic approach ($\Omega_i\Delta t \gg 1$) [13] will be examined in future studies. A weak point of the GK modeling is the absence of the polarization drift movement. This weak point can be solved by the DLF method.

References

[1] J.P. Verboncoeur, Plasma Phys. Control. Fusion **47**, A231 (2005).
[2] T. Takizuka, Plasma Phys. Control. Fusion **59**, 034008 (2017).
[3] T. Takizuka, Plasma Sci. Technol. **13**, 316 (2011).
[4] K. Ibano, S. Togo, T. Lang, et al. Contrib. Plasma Phys. **56**, 705 (2016).
[5] K. Ibano, Y. Kikuchi, S. Togo, Y. Ueda, T. Takizuka, Nucl. Fusion **59**, 076001 (2019).
[6] S. Togo, T. Takizuka, M. Nakamura, et al., J. Comput. Phys. **310**, 109 (2016).
[7] S. Togo, T. Takizuka, D. Reiser, et al., Nucl. Fusion **59**, 076041 (2019).
[8] J.P. Boris, Proc. 4th Conf. on Numerical Simulation of Plasmas, p.3 (1970).
[9] T. Takizuka, K. Ibano, S. Togo, Plasma Fusion Res. **16**, 1203100 (2021).
[10] T. Takizuka, H. Abe, J. Comput. Phys. **25**, 205 (1977).
[11] T. Takizuka, K. Ibano, M. Yagi, Plasma Fusion Res. **13**, 1203088 (2018).
[12] T. Takizuka, K. Ibano, M. Yagi, Plasma Fusion Res. **14**, 1203091 (2019).
[13] X. Garbet, Y. Idomura, L. Villard, T.H. Watanabe, Nucl. Fusion **50**, 043002 (2010).

Development of an integrated model GOTRESS+ and its application to assessment of JT-60SA operation scenarios including the pedestal

M. Honda, N. Aiba, *H. Seto, E. Narita and N. Hayashi

Kyoto University, Nishikyo-ku, Kyoto 615-8530 Japan

National Institutes for Quantum Science and Technology, Naka, Ibaraki 311-0193 Japan

**National Institutes for Quantum Science and Technology, Rokkasho, Aomori 039-3212 Japan*

The integrated model GOTRESS+ with EPED1

A steady-state transport equation solver, GOTRESS [1,2], has been developed, which benefits from global optimization techniques such as a genetic algorithm and the Nelder-Mead method such that they directly find the solution where a transport flux matches an integrated source. We have developed a novel integrated model GOTRESS+, mainly consisting of GOTRESS, the equilibrium and current profile solver ACCOME and the neutral beam (NB) heating code OFMC for predictions of temperature profiles consistent with an equilibrium and heating profiles. For the development of operation scenarios in JT-60SA, ITER and a DEMO reactor, it is indispensable to predict the pedestal, which accounts for a large proportion of plasma stored energy in an H-mode plasma. Recently the EPED1 model [3] has been incorporated into GOTRESS+ for predictions consistent between the core and the pedestal plasmas. The EPED1 model is based on the hypothesis that the pedestal is determined by two constraints: the peeling-ballooning stability, and the empirical scaling of the pedestal height observed in DIII-D, the latter of which relies on the kinetic ballooning turbulence theory. Our own EPED1 model works together with ACCOME as an equilibrium solver and the MHD stability code MARG2D [4]. The flowchart of a GOTRESS+ execution can be seen in Fig. 1. The workflow is regulated by the Python script with the aid of a job scheduler installed in the machine where GOTRESS+ runs. GOTRESS+ is now extended to predict the plasma profiles entirely inside the plasma, provided that the density profiles are given.

Application of GOTRESS+ to JT-60SA plasmas

With the CDBM transport model used, GOTRESS+ has been applied to the development of two operation scenarios in JT-60SA: an ITER-like inductive operation scenario (#4-1) and a high β_N fully non-inductively current driven operation scenario (#5-1), where β_N is the normalized beta. We here demonstrate the latter one: $B_T = 1.72\mathrm{T}$, $I_p = 2.3\mathrm{MA}$, $P_{NB} = 16\mathrm{MW}$ and $P_{EC} = 7\mathrm{MW}$. The setting of the plasma parameters is targeted at developing the DEMO-relevant plasma regimes in a steady state without the inductive current. In general, it is difficult to simultaneously achieve them in a self-consistent manner, as all the current must be sustained by the current drive of the auxiliary heating systems and the bootstrap current, and the MHD stability must also be met. The boundary of GOTRESS is set at $\rho = 0.8$ and outside of it the profiles are determined by EPED1.

As shown in Fig. 2, the GOTRESS+ simulation revealed that the consistent solution could be obtained, which satisfied all of the target parameters such as $\beta_N = 4.33(> 4.3)$, the energy confinement improvement $H_{98(y,2)}$ of $1.61(> 1.3)$ and the bootstrap current fraction f_{BS}~$0.68(\sim 0.68)$[5]. Of course, the plasma was MHD stable. The double barrier structure of the given density profile makes it possible to attain the solution. The negative magnetic shear in conjunction with the alpha stabilization suppresses the turbulent transport in the core region and forms the ITBs, which bring about the steep pressure gradients and the resultant high f_{BS}.

Currently the implementation of alpha heating due to fusion reactions in GOTRESS+ is in progress for the purpose of predicting DEMO plasmas.

References

[1] M. Honda, Comput. Phys. Commun. **231**, 94 (2018).

[2] M. Honda and E. Narita, Phys. Plasmas **26**, 102307 (2019).

[3] P. B. Snyder et al., Phys. Plasmas **16**, 056118 (2009).

[4] N. Aiba et al., Comput. Phys. Commun. **175**, 269 (2006).

[5] M. Honda et al., Nucl. Fusion **61**, 116029 (2021).

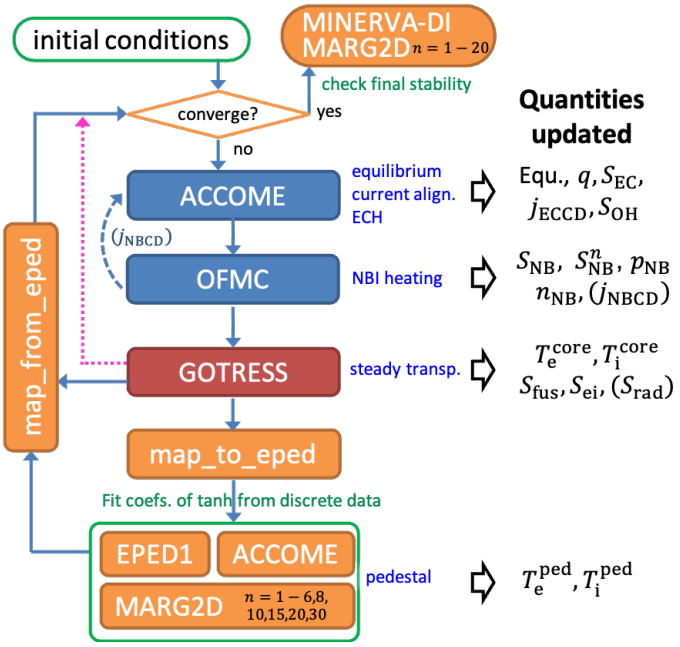

Fig. 1: Flowchart of a GOTRESS+ execution with EPED1.

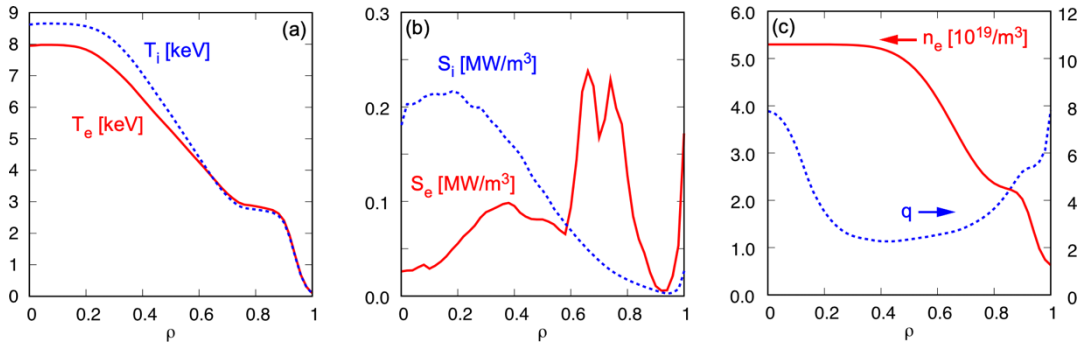

Fig. 2: Final state of (a) the electron and ion temperature profiles, (b) the electron and ion heat sources and (c) the electron density and the safety factor profiles for #5-1.

Evaluation of heating power required for L–H transition in JA DEMO

S. Sugiyama, N. Aiba, N. Asakura, N. Hayashi, Y. Sakamoto,
and Joint Special Design Team for Fusion DEMO

National Institutes for Quantum Science and Technology

1 Introduction

In the DEMO reactor, it is desirable to reduce the volume of the ports for the heating and current drive components from the viewpoint of tritium breeding. It is necessary to clarify the role of the heating and current drive in each phase of a plasma operation and to evaluate the required heating power. In JA DEMO [1], which is a design concept of a tokamak DEMO reactor, the total heating power of 80–150 MW can be prepared from the study of tritium breeding. The H-mode operation is essential to obtain high-performance burning plasmas; the L–H transition is a stage requiring high heating power and should be completed within the heating power injected in the steady burn phase.

The heating power required for the L–H transition can be evaluated by comparing the loss power from the plasma with the threshold power. Since the density evolution during the transition and the back transition conditions are not fully understood, assumptions on these are necessary to evaluate the required heating power. The higher heating power is required when the density rise time is shorter because of the increase of the change rate of the plasma stored energy, $\mathrm{d}W/\mathrm{d}t$ [2]. In DIII-D and ASDEX Upgrade, the H-mode can be maintained even when the loss power drops to half of the threshold power, while in JET, no or weak hysteresis has been observed. It has been pointed out that $\mathrm{d}W/\mathrm{d}t$ should not be subtracted from the loss power after the L–H transition [3]; however, it is safer to consider the effect of $\mathrm{d}W/\mathrm{d}t$ and assume no hysteresis for evaluating the heating power required for the L–H transition of the DEMO reactor.

To reduce the heat load on the divertor, the loss power should be controlled below the allowable value by impurity injection. It is necessary to consider the scenario such that the L–H transition and the divertor heat load are compatible by adjusting heating power and the impurity amount.

We have investigated the dependence of the heating power required for the L–H transition on the density rise time and the control of the loss power by using Ar injection in JA DEMO.

2 Analysis model

An L–H transition model was introduced into the TOPICS code [4]. The threshold power, P_{TH}, is obtained from Martin's fitting expression [5] and multiplied by 0.8 to consider the ion mass dependence. The L–H transition is started when the net loss power across the separatrix, P_{sep}, exceeds P_{TH}. Here, P_{sep} is defined as the absorbed heating power minus the radiation power and $\mathrm{d}W/\mathrm{d}t$. The temperature profile is solved with the prescribed density profile evolution and the CDBM model. The H-mode temperature profile outside the normalized minor radius, ρ, of 0.85 is fixed using the pedestal profile model [6]. The pedestal profile during the L–H transition is determined so that the L- and H-mode profiles are smoothly connected taking a prescribed pedestal formation time, Δt_{ped}. The impurity ion density profile in the core region is solved by giving the time evolution of the density at the separatrix.

The density profile was assumed to be $[4(1-\rho^2)^{0.6}+1]\times 10^{19}$ m^{-3} in the L-mode and the flat profile

with the Greenwald density fraction of 0.85. Argon was considered as the impurity. The anomalous diffusion coefficient of 2.2 m^2/s and the pinch velocity of -0.28ρ m/s were assumed for argon ions.

3 Results and discussion

Figure 1 shows the time evolution of P_{sep} for $\Delta t_{ped} = 5$ s. After the plasma current reaches the flat top, NB is injected from 66 s and the L–H transition occurs at 70.5 s. The loss power drops by the increase of dW/dt after the transition started; in this case, the back transition occurs if no hysteresis exists.

Figure 2 shows the Δt_{ped} dependence of the minimum value of P_{sep}/P_{TH} during the transition. The higher heating power allows the shorter transition time. If the density can be controlled so that the transition takes 18 seconds, the transition is achieved without hysteresis with the NBI power of 80 MW.

Figure 3 shows the dependence of P_{sep}/P_{TH} during the transition on Ar density fraction at the separatrix, f_{Ar}. The loss power decreases as the radiation power increases by impurity injection. When the impurity amount is too much, P_{sep} drops below P_{TH}. The loss power cannot be suppressed by increasing the impurity amount in the case of the high NBI power. By selecting an appropriate combination of impurity amount and NBI power, P_{sep}/P_{TH} can be controlled to be almost constant.

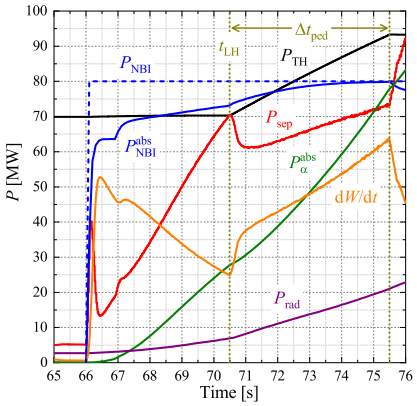

Fig. 1 Time evolution of P_{sep}.

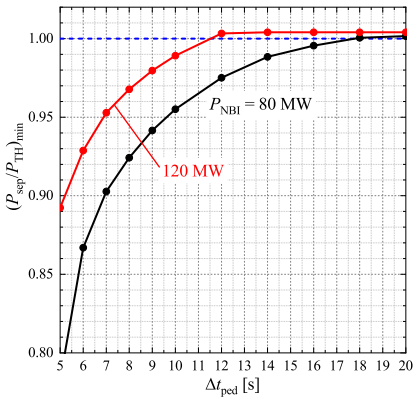

Fig. 2 Dependence of the minimum value of P_{sep}/P_{TH} on Δt_{ped}.

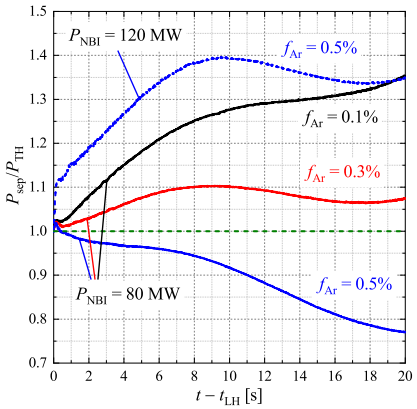

Fig. 3 Dependence of P_{sep}/P_{TH} on f_{Ar}.

4 Conclusion

We have investigated the heating power required for the L–H transition of JA DEMO, introducing the L–H transition model into the TOPICS code. The required heating power varies depending on the density rise time and the back transition condition. By adjusting the heating power and impurity density fraction, it is possible to control P_{sep} and achieve both L–H transition and reduction of the divertor heat load. We have obtained the prospect that the L–H transition is possible within the heating power supposed in the current design activities of JA DEMO. Our future work is to evaluate the specific heating power required for the L–H transition, improving the model to describe the density and temperature evolutions.

[1] K. Tobita, et al., Fusion Eng. Des. **136** (2018) 1024.
[2] C. Kessel, et al., Nucl. Fusion **55** (2015) 063038.
[3] O. Mitarai, et al., Fusion Eng. Des. **55** (2001) 477.
[4] N. Hayashi, et al., Phys. Plasmas **17** (2010) 056112.
[5] Y. Martin, et al., J. Phys.: Conf. Ser. **123** (2008) 012033.
[6] J. Garcia, et al., Nucl. Fusion **54** (2014) 093010.

Progress of wave analyses in toroidal plasmas using the integrated code suite TASK

Atsushi Fukuyama
Professor Emeritus, Kyoto University, Kyoto, Japan

There are various applications of wave in plasmas for control of plasma by waves including plasma production, heating, current drive and rotation generation, and for diagnostics of plasma by waves including Bremsstrahlung and synchrotron radiation, wave cutoff and interference, scattering of waves by fluctuation, and excitation by energetic particles. Various modules for wave modeling and analysis have been implemented in the integrated code TASK:

Modules related to wave analysis in TASK

DP	dielectric tensor (cold, Maxwellian, arbitrary f, relativistic)
WR	geometrical optics (ray tracing, beam tracing)
WM	full wave optics (Fourier expansion, differential)
WF	full wave optics (finite element method, integro-differential)
FP	velocity distribution function (kinetic transport, kinetic wave)

1 DP

Recent progress in wave dispersion analysis using DP has been made in the implementation of perpendicular cold beam contribution in the dielectric tensor. It has been applied to the analysis ion cyclotron emission by NBI in LHD plasmas, and the dispersion relation and the growth rate shown in Fig. 1 are consistent with PIC simulation by Dr. Toida.

2 WR

Recent ECCD analysis for ITER plasma using the full-relativistic numerical estimate of the anti-Hermite term of dielectric tensor has suggested that the down-shifted second-harmonic EC resonance strongly absorb the EC waves in high-temperature central plasma. Therefore low-field-side horizontal injection is not efficient for ECCD in the central plasma (see Fig. 2), and top-launch injection is promising for ECCD in the central and inner region of reactor plasma.

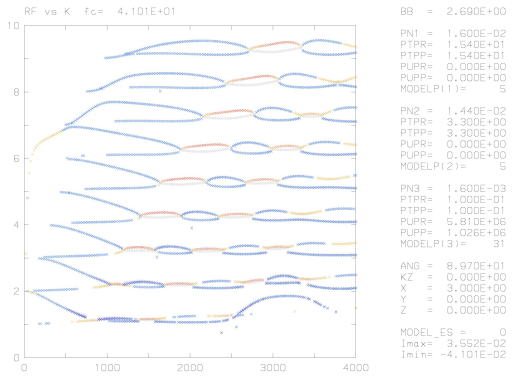

Fig. 1: Dispersion relation obtained by TASK/DP for the ion cyclotron emission driven by NBI in LHD

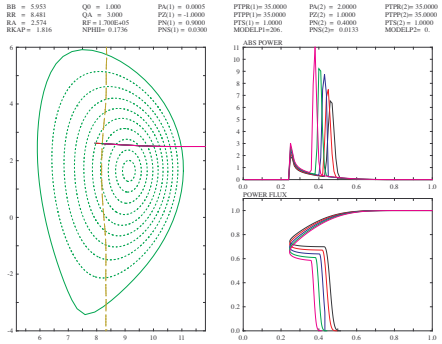

Fig. 2: Strong second-harmonic absorption in high $T_e(0) = 35$ keV plasma prevents efficient ECCD due to relativistic downshift of $\omega = 2\omega_{ce}$ resonance

3 WM

Improvement of mode-expansion full wave code TASK/WM for the analysis of ICRF heating in LHD plasma is under way. More poloidal mode numbers are required for accurate description of wave structure in helical plasmas.

4 WF

There are several versions of FEM full wave modules in TASK:

Modules for FEM full wave analysis in TASK

W1	1D	hot	O-X-B mode conversion of EC waves in tokamaks
WF2	2D	cold	Helicon wave excitation in cylindrical plasmas
WF2D	2D	cold	O-X mode conversion EC waves in LHD plasmas
LH, Slow wave of IC			
WF3D	3D	cold	IC waves in tandem mirror configuration

In order to describe the kinetic effects of plasmas in the full wave analysis using the finite element method (FEM) requires the integro-differential analysis which is free from wave number. We have formulated the integro-differential dielectric tensor for unmagnetized plasmas (laser-plasma interaction), magnetized longitudinal (magnetic beach heating) and magnetic transverse (finite Larmor radius effects).

Accurate analysis of O-X-B mode conversion of EC wave requires kinetic full wave analysis because both evanescent region and Bernstein waves have to be taken into account. Figure 3 shows the wave structure of the EC wave in a slab plasma simulating tokamak plasma. The EC wave is excited as an O-mode (E field parallel to the external magnetic field in z direction) by an wave guide antenna located near the lower corner on the low-field low-density right-hand-side wall. The O-mode with optimum injection angle is mode-converted to the X-mode near the O-mode cutoff. The X-mode is reflected to the shorter wave-length X-mode in the high-density region, and it is reflected again at the upper-hybrid-resonance layer and converted to the very-short wave-length Bernstein mode which is absorbed at the fundamental cyclotron resonance or by collision damping. Though the O-X-B mode conversion efficiency is similar to the cold O-X mode conversion efficiency, the mode structure the Bernstein wave was first obtained by the integro-differential full wave analysis.

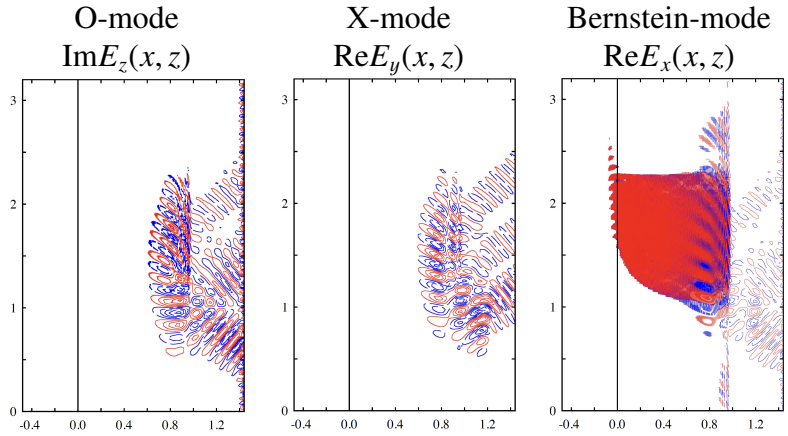

Fig. 3: Kinetic full wave analysis of O-X-B mode conversion of EX waves in a slab plasma

Development of control system for fusion plasmas using data assimilation

Y. Morishita[1], S. Murakami[1], M. Yokoyama[2,4], G. Ueno[3,4,5]

[1]*Department of Nuclear Engineering, Kyoto University, Nishikyo, Kyoto, 615-8540, Japan*
[2] *National Institute for Fusion Science, National Institutes of Natural Science, Toki 509-5292, Japan*
[3]*The Institute of Statistical Mathematics, Research Organization of Information and Systems, Tokyo 190-8562, Japan*
[4]*The Graduate University for Advanced Studies, SOKENDAI, Toki 509-5292 and Tokyo 190-8562, Japan*
[5]*The Joint Support-Center for Data Science Research, Tokyo 190-0014, Japan*

1. Introduction

To develop a numerical system that can control the behavior of fusion plasmas with high accuracy, we are developing a data assimilation system, ASTI[1,2], based on the integrated transport simulation code, TASK3D[3]. Data assimilation can also improve simulation models involving turbulence models. As data assimilation methods, We use the ensemble Kalman filter (EnKF) to predict the behavior of fusion plasmas and the ensemble Kalman smoother (EnKS) to estimate the models which can reproduce experimental data. We have developed a new control method for fusion plasmas using data assimilation. In this paper, the results of numerical experiments to control the LHD plasma using the proposed method are shown.

2. Data assimilation system

ASTI is a data assimilation system which employs the integrated transport simulation code, TASK3D as the system model. ASTI can assimilate the experimental time series data into the integrated simulation to predict and analyze the behavior of fusion plasmas. We have extended ASTI to a control system by implementing the control method.

The proposed control algorithm consists of two components. The first is a filter for control, which estimates the control input $\mathbf{u}^*$ to achieve the target state $\mathbf{z}$ and computes the predicted distribution under the control. This filter finds the optimal control $\mathbf{u}^*$ by assimilating $\mathbf{z}$ to the predicted distribution and calculates the predicted distribution under the control by assimilating $\mathbf{u}^*$. This filter is assumed to be executed at Δt_z intervals.

The second is a filter for observation, which optimizes the state vector using the observation data obtained sequentially. In a situation where the observations are obtained at Δt_y intervals ($\Delta t_y > \Delta t_z$), it is required to assimilate the observations separated in time, because the time at which the observation are obtained and the time of the latest prediction in numerical space differ by Δt_y. This can be achieved by assimilating the observation at a time t, $\mathbf{y}_t$, to the joint distribution of the two time points, $p(\mathbf{x}_t, \mathbf{x}_{t+\Delta t_y})$.

3. Simulation results

A numerical experiment is conducted to investigate the control performance by controlling the virtual LHD plasma (TASK3D). We consider controlling the ECH input power to make the electron temperature follow the target state time series as shown in Figure 1. The ECH input power is adjusted by ATSI in the range 0.5 - 5 MW in 0.5 MW increments ($\Delta t_z = 0.1$ s). We take the electron temperature at the plasma center ($\rho = 0$) as the target state

z and assume that the radial profiles of electron temperature and ion temperature can be observed in the cycle of $\Delta t_y = 0.5$ s. The electron density at the center is assumed to be 1.0×10^{19} m^{-3} . The state vector consists of electron temperature, ion temperature, ECH input power, and numerical factors for thermal turbulent diffusivity of electron and ion. This numerical experiment is performed by 400 ensemble members. Different models of electron thermal turbulent diffusivity in ASTI and virtual plasma are assumed. Gyro-Bohm model and the model that averages gyro-Bohm model and Alcator model are assumed in ASTI and the virtual plasma, respectively.

Figure 2 shows the simulation results of the electron temperature controlled by ASTI. It can be seen that the electron temperature under the control (green curve) agrees well for the target state time series (red curve). We have confirmed that the numerical factor for thermal turbulent diffusivity is optimized to bridge the differences between the models in ASTI and the virtual plasma.

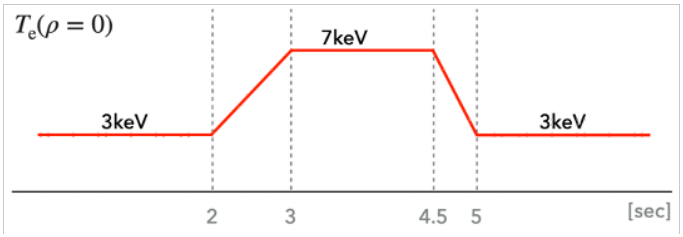

Fig. 1 Target state time series of electron temperature at the plasma center.

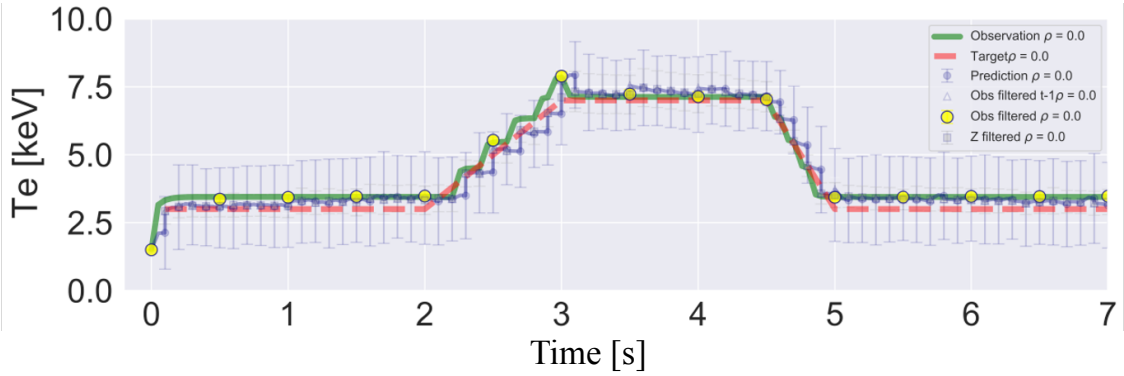

Fig. 2 Simulation results of the electron temperature controlled by ASTI.

4. Summary

We are developing the data assimilation system, ASTI to analyze and control the behavior of fusion plasmas in real time. We have developed the control algorithm using data assimilation and implemented it in ASTI. The numerical experiment has been conducted to demonstrate the performance of the control method. ASTI is expected to be a robust system for analysis, prediction, and control of fusion plasma that connects an actual plasma and a plasma in numerical space.

References

[1] Y. Morishita, *et al*., Computer Physics Communications **274**, 108287 (2022).
[2] Y. Morishita, *et al*., Nuclear Fusion **60**, 056001 (2020).
[3] S. Murakami, *et al*., Plasma Phys. Control. Fusion **57**, 119601 (2015).

Implementation of Finite Orbit Width Bounce-averaged Fokker-Planck Simulation Code TASK/FP

Akiyoshi Anzai, Keigo Ota, Atsushi Fukuyama, Mitsuru Honda, Sadayoshi Murakami

Department of Nuclear Engineering, Kyoto University, Nishikyo, Kyoto, 615-8140, Japan

1 Introduction

In a fusion DEMO reactor, it is necessary to accurately simulate the plasma behaviors in order to construct an efficient start-up scenario of burning plasma. Currently, fusion reactor simulation codes are being developed in many countries, and research is being conducted to improve the accuracy of the simulation scheme and to reduce the computation time. One way to simulate plasmas is to solve the magnetohydrodynamic equation, but this is not sufficient to describe the behavior of energetic particles. It is necessary to solve the kinetic equation describing the behavior of the distribution function of plasma species including energetic particles (EPs).

In an axisymmetric magnetic confinement system such as tokamak, bounce-averaged Fokker-Planck equation (FP) where the distribution function is averaged over the particle gyro motion, the bounce motion in a magnetic mirror, and the axisymmetric direction, has been introduced[1]. The bounce-averaged FP code TASK/FP was developed to analyze the behavior of the velocity distribution function in toroidal plasmas, and has been employed to analyze the interaction of plasmas with various waves and toloidal electric fields in the presence of various collision models[2]. However, the conventional TASK/FP analysis uses an approximation that neglects the orbit width of the particles. As a result, the behavior of EPs with large orbit width cannot be described accurately.

2 Original TASK/FP code

In the original TASK/FP code, we use the bounce-average FP equation with zero orbital width and calculate time evolutions of the constants of motion(COM) in the midplane. The bounce-average FP equation is the kinetic equation which is averaged over for three time scales, firstly gyro-phase, secondly bounce-phase, and thirdly toroidal angle[1][3]. On the assumption that gyro-phase and bounce-phase are shorter than the time scale of other interest plasma variations, these average operations are applied. As a result, we can reduce 3 dimensions in the kinetic equation, and obtain the following Fokker-Planck equation in the COM space.

$$\frac{\partial}{\partial t}\mathcal{J}_I f(\boldsymbol{I},t) = \frac{\partial}{\partial I_i}\mathcal{J}_I\left[D^{ij}\frac{\partial}{\partial I_j} - F^i\right]f(\boldsymbol{I},t) + \mathcal{J}_I H(\boldsymbol{I}) \tag{1}$$

$$D^{ij} = \left\langle \frac{\partial I^i}{\partial \boldsymbol{u}} \cdot \boldsymbol{D^{uu}} \cdot \frac{\partial I^j}{\boldsymbol{u}} \right\rangle \tag{2}$$

$$F^i = \left\langle \frac{\partial I^i}{\partial \boldsymbol{u}} \cdot \boldsymbol{F^u} \right\rangle \tag{3}$$

Here f is distribution function of particles, $\mathcal{J}$ is jacobian, $\boldsymbol{I} = (I_1, I_2, I_3)$ is three components COM vector, D^{ij} is the diffusion coefficient, F^i is the advection coefficient and H is the source term. $\boldsymbol{D^{uu}}$ is the diffusion tensor and $\boldsymbol{F^u}$ is the advection vector in a local space $\boldsymbol{u}$. The notation $\langle\rangle$ denotes the bounce-average. The summation convention implied. Hereafter, the bounce-average operation is to be taken over poloidal motion and $\langle\rangle$ is

$$\langle\rangle = \frac{1}{\tau_p}\int_0^{\tau_p} dt \tag{4}$$

where τ_p is the bounce time on the drift orbit.

As COM variable, we choose the set $\boldsymbol{I} = (\epsilon, \mu, P_\xi)$ in which ϵ is the energy, μ is the magnetic moment, and P_ξ is the canonical toloidal angular momentum. However, these variables are inconvenient to calculate the time evolution of distribution functions because these variables do not contain isolated configuration space coordinates, and also the momentum p is mixed in P_ξ. This causes the difficulty in computational grids.

In terms of computational grids, the set $\boldsymbol{I} = (p, \theta_0, \rho_0)$ is used in TASK/FP[2]. Here, p is the momentum, θ_0 is the pitch angle at a minimum magnetic field, and ρ_0 is the minor radius at a minimum field. Using these COM, the set (ϵ, μ, P_ξ) is derived from $\boldsymbol{I} = (p, \theta_0, \rho_0)$. Another merit using this COM space is that the relation between these variables and orbits are obvious. For each ρ_0 point, the values of particle momentum p and pitch angle θ_0 determine one orbit.

In TASK/FP, the diffusion tensor $\boldsymbol{D^{uu}}$ and the advection vector $\boldsymbol{F^u}$ at a local space $\boldsymbol{u} = (p, \theta, \rho, \phi)$ are averaged over particle orbits, which have zero orbital width. Here, p is the momentum, θ is the pitch angle at the minimum field, ρ is the minor radius, and ϕ is the poloidal angle. The tensor and vector driven by Coulomb collision can be expressed as

$$\boldsymbol{D^{uu}} = \begin{bmatrix} D_{pp} & D_{p\theta} & 0 \\ D_{\theta p} & D_{\theta\theta} & 0 \\ 0 & 0 & 0 \end{bmatrix}, \quad \boldsymbol{F^u} = \begin{bmatrix} F_p \\ F_\theta \\ 0 \end{bmatrix}. \tag{5}$$

Zero orbital width approximation causes that radial variations of the diffusion tensor and advection vector due to collisions, are not taken into account. The radial variable is constant in the original FP code. Therefore we cannnot evaluate the radial transport due to collision and the radial broadening of the collisional energy transfer.

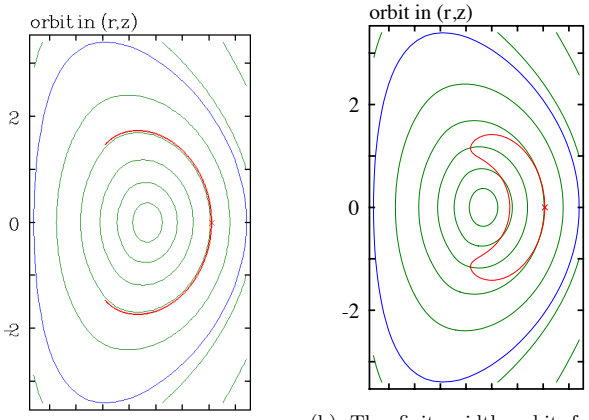

(a) Zero width orbit

(b) The finite-width orbit for a trapped particle

Fig. 1: The Particle orbits in the tokamak

In the following section, we introduce the FOW variables into TASK/FP and consider some conditions to solve these problems.

3 Introduction of FOW variables

To introduce FOW effects into TASK/FP, we changed variables (p, θ_0, ρ_0) to the new COM space $I = (p, \theta_m, \rho_m)$. Here, p is the momentum, θ_m is the pitch angle at the maximum poloidal magnetic flux ψ_m, ρ_m is the minor radius at ψ_m of an orbit. This is the difference between our study and the previous work by Petrov[4]. In the new COM space, the transform matrix is given by.

$$\frac{\partial \boldsymbol{I}}{\partial \boldsymbol{u}} = \begin{bmatrix} \frac{\partial p}{\partial p} & \frac{\partial p}{\partial \theta} & \frac{\partial p}{\partial \rho} \\ \frac{\partial \theta_m}{\partial p} & \frac{\partial \theta_m}{\partial \theta} & \frac{\partial \theta_m}{\partial \rho} \\ \frac{\partial \rho_m}{\partial p} & \frac{\partial \rho_m}{\partial \theta} & \frac{\partial \rho_m}{\partial \rho} \end{bmatrix} \tag{6}$$

To obtain $\partial \boldsymbol{I}/\partial \boldsymbol{u}$ and the jacobian $\mathcal{J}$, we calculate these mathematical quantities (ϵ, μ, P_ξ) for $\boldsymbol{u} = (p, \theta, \rho, \phi)$,which are written as

$$\epsilon = \sqrt{m^2c^4 + |\boldsymbol{p}|^2c^2} - mc^2 \tag{7}$$

$$\mu = \frac{1}{2}\frac{p^2\sin^2\theta}{mB(\rho,\phi)} = \frac{1}{2}\frac{p^2\sin^2\theta_m}{mB_m} \tag{8}$$

$$P_\xi = \frac{F(\rho,\phi)}{B(\rho,\phi)} p\cos\theta - q\psi(\rho) = \frac{F_m}{B_m} p\cos\theta_m - q\psi_m. \tag{9}$$

where m is the mass of a particle, c is the speed of light, $\psi(\rho)$ is the magnetic flux at ρ, and q is the charge. $F = RB_\phi$ denotes poloidal currents where R is the toloidal radius, and B_ϕ is the toroidal field. These conserved quantities are wrote down.

$$p = p \tag{10}$$

$$\frac{\sin^2\theta}{B(\rho,\phi)} = \frac{\sin^2\theta_m}{B_m} \tag{11}$$

$$\frac{F(\rho)}{B(\rho,\phi)} p\cos\theta - q\psi(\rho) = \frac{F_m}{B_m} p\cos\theta_m - q\psi_m \tag{12}$$

Using these relations, the transform matrix can be obtained. Hereafter, the prime indicates the deivative with respect to $\partial/\partial\rho_m$.

In the kinetic equation, like the Boltzmann equation, the variables of the distribution function are in the phase space $(\boldsymbol{x}, \boldsymbol{p})$. On the other hand, for computational grids, we use the new COM $I = (p, \theta_m, \rho_m)$, which conserves (ϵ, μ, P_ξ). Therefore, the jacobian should be expressed in those three variable spaces.

We transform the variables $(\boldsymbol{x}, \boldsymbol{p})$ to $(\boldsymbol{z}, \tilde{\boldsymbol{z}})$, where $\boldsymbol{z} = (\epsilon, \mu, P_\xi)$, $\tilde{\boldsymbol{z}} = (\phi, \xi, \Theta)$ and Θ is the gyro phase.Then, we average over $\tilde{\boldsymbol{z}}$ and transform $\boldsymbol{z}$ to the new COM space (p, θ_m, ρ_m). Finally, the jacobian for the transformation from $(\boldsymbol{x}, \boldsymbol{p})$ to (p, θ_m, ρ_m) is expressed as

$$\mathcal{J}_I = \frac{4\pi^2\tau_p}{m^2|q|} \cdot \frac{p^3 \sin\theta_m}{m^2 B_m \sqrt{1+(\frac{p}{mc})^2}} \cdot \left[\frac{p}{B_m^2}\left\{(F_m' B_m - F_m B_m')\cos^2\theta_m - \frac{1}{2}F_m' B_m \sin^2\theta_m\right\} - q\psi_m' \cos\theta_m\right]. \tag{13}$$

4 Orbit classifications

When we use the zero orbital width approximation, we neglect the effects of collisional variations of drift orbits. However, with the FOW effects, it is necessary to classify orbits and to evaluate the variation of them since the diffusion and advection coefficients are obtained by integrating over the bounce motion.

There are several previous papers on the orbit classification[5][6]. According to Rome and Peng (1979)[5], the orbit region is classified into 4 regions with ψ_m by unique COM space surfaces. Figure2 shows the

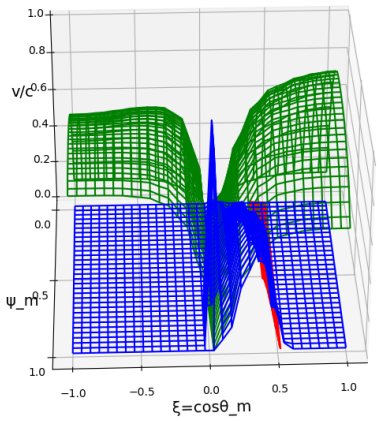

Fig. 2: Orbit classification with orbit surfaces

surfaces in the 3D COM space represented by $(v/c, \cos\theta_m, \psi_m)$. The green surface separates the passing and forbidden regions, and the blue one the passing and trapped regions. The stagnation orbit on the green surface includes the point where $v_Z = 0$ and are fragile for collisional perturbation. Figure3 shows the cross-section at $\psi_m = 0.63$.

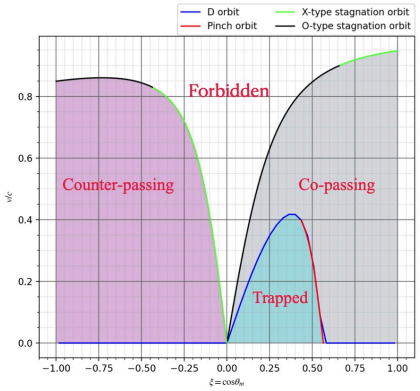

Fig. 3: Orbit region at $\psi_m = 0.63$

5 Conditions on the orbit boundaries

As discussed in the previous section, it is necessary to set the proper boundary condition on pinch orbits in order to conserve particle numbers. The COM variables may change discontinuously when the particle cross the pinch orbit surface. Figure4 shows the change of the COM variables in phase space and Figure5 show the change of the particle orbit in real space. Figure4 and figure5 show the orbit variation due

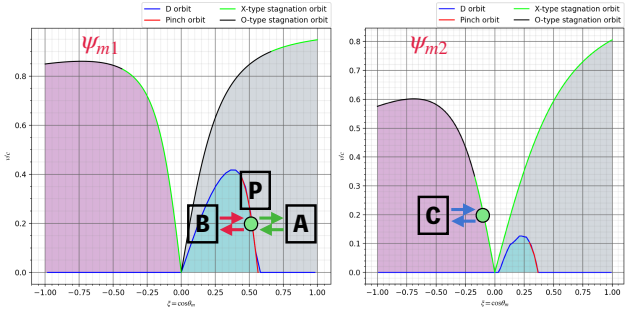

Fig. 4: Particle flux and orbital boundaries

to the collision. In fig4, the each point A, B, C, P corresponds to the orbit A (co-passing), B (trapped), C (counter-passing), and P (pinch) respectively. Small collision perturbation on the orbits may cause the transition between orbit regions represented by arrow. It should be noted the particle flux from the trapped region (red) has to be equal to the sum of the flux to the co-passing region (green) and the one to the counter-passing region (blue).

6 Comparison of particle diffusion estimates

We compare the diffusion coefficient of the FOW FP code with the diffusion coefficient of the neoclassical theory. In order to evaluate only the diffusion coefficient, we set the advection therm as zero and the source term are neglected. Figure6 shows the radial diffusion coefficients of the electron and the deuterium ion as a function of minor radius. The radial diffusion coefficients are evaluated by the ratio of the particle flux and the density gradient. For FOW cases, the radial diffusion is caused by orbit change due to collisional velocity change. For neoclassical estimates, the neoclassical radial diffusion is averaged over the bounce orbit. The FOW results are the same order with the neoclassical estimates, and shows larger diffusion near the magnetic axis and smaller near the peripheral. The origin of the discrepancy requires further analysis of the FOW effects.

7 Summary and future works

The FOW effect has successfully been introduced in TASK/FP. The schemes to properly classify orbits and set boundary conditions have been implemented. Radial diffusion coefficients of FOW became larger than the conventional neoclassical estimates near the magnetic axis.

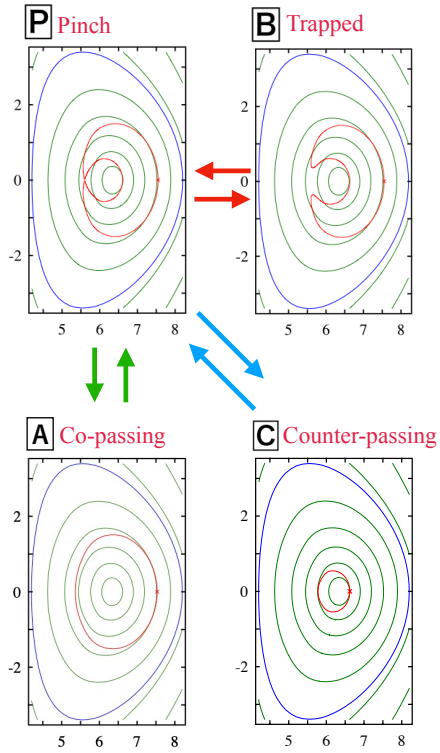

Fig. 5: Orbit shapes at each points

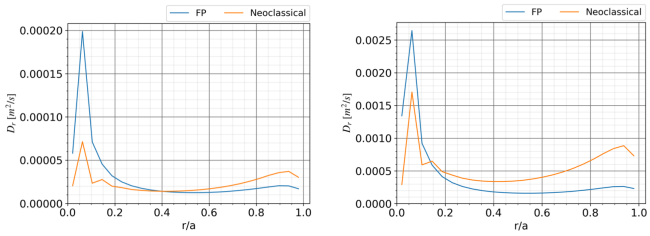

(a) Radial diffusion coefficients of electron

(b) Radial diffusion coefficients of deuterium ion

Fig. 6: Diffusion coefficient of FOW and neoclassical theory

There is a possibility that the dependence is due to the potato orbit effects. In the following study, we implement the NBI heating term into the FOW TASK/FP and evaluate the FOW effects.The effort to reduce computation time by parallel processing in the presence of FOW is under way.

References

[1] M.G.McCoy A.A.Mirin J.Killeen, G.D.Kerbel. *Computational Methods for Kinetic Models of Magnetically Confined Plasmas*. Springer-Verlag, 1986.

[2] H.Nuga and A.Fukuyama. *Progress in nuclear science and technology*, 2:78–84, 2011.

[3] K.Kupfer. *Proc.IAEA Technical Committee Meeting on Fast Wave Current Drive in Reactor Scale Tokamaks*, page 149, 1991.

[4] Y.V.Petrov and R.W.Harvey. *Plasma Phys. Control. Fusion*, 58:115001, 2016.

[5] J.A.Rome and Y.M.Peng. *Nuclear Fusion*, 19:1193–1205, 1979.

[6] M.Okamoto S.Satake, H.Sugama and M.Wakatani. *Plasma Phys. Control. Fusion*, 77:573–585, 2001.

A BOUT++ extension for full annular tokamak edge turbulence simulation

SETO Haruki[1)], DUDSON Benjamin Daniel[2,3)], XU XueQiao[2)], YAGI Masatoshi[1)]

1) QST, 2) LLNL, 3) U. York

It is one of key issues for ITER and DEMO to understand the dynamics of edge localized modes (ELMs) [1] in metal wall devices. This is because intermittent heat fluxes triggered by ELMs should be avoided or mitigated to levels low enough to remain within heat load constraints on plasma facing components [2].

In H-mode discharges with moderate to high D_2 gas puff rate in JET ITER-like wall (JET-ILW), which is required for W control for stable H-mode operations, the increase of neutral gas pressure degrades pedestal temperature, and the operation point is in ballooning mode branch where the high-n pressure-gradient driven instabilities determine the operation point like type-III ELMs [3]. Here n is the toroidal mode number. This is qualitatively different from type-I ELMs driven by moderate-n peeling-ballooning mode.

On the other hand, it is reported that a highly reproducible stationary small ELM regime is observed in EAST experiments, which is suitable for future steady-state fusion devices [4]. The small ELM is a kind of grassy ELM, but its operation point is in the low-n peeling mode branch rather than the high-n ballooning branch like grassy ELMs in JT-60U [5]. The nonlinear simulations show that the key mechanism for the grassy ELM in EAST is the expansion of the peeling boundary due to radially localized steepening of pedestal pressure gradient by a radially localized collapse. Further verification study is required in both experiments and simulations to elucidate the mechanism of grassy ELM in EAST.

It is therefore important for understanding physics of ELMs in metal wall devices including ITER and DEMO to develop a nonlinear reduced MHD code solving off-resonant (n=0), low-n (n~1), moderate-n (n>1) and high-n (n>>1) modes simultaneously. In this work, an edge MHD/turbulence code for solving interplay among off-resonant, low-n, moderate-n and high-n modes using BOUT++ framework [6] is developed.

BOUT++ employs both field-aligned coordinates [7] and flux-surface coordinates for tokamak edge simulations in combination with the radial derivative method and the shifted metric method to simulate ballooning mode instabilities with reasonable computational cost and high accuracy. It has provided qualitative understandings on ELMs triggered by middle-n ~ high-n ballooning modes [8]. Taking fluctuation-driven n=0 and very low-n flow and magnetic field however has been an open issue due to the numerical problem in the flute-ordered Poisson solver required for BOUT++ coordinates.

These limitations have been partially removed by the flute-ordering-free Poisson solver designed for n=0 mode [9] which enables BOUT++ to simulate an interplay between fluctuation driven n=0 net flow and MHD turbulence during ELM crash triggered by middle-n ~ high-n ballooning modes. In our previous works [10,11], it is revealed that the zonal net flow generated during the pedestal collapse can trigger subsequent turbulence bursts accompanied with cyclic oscillations between pressure gradient, zonal flow and turbulence and enhance turbulent energy transport after the pedestal collapse. This framework however has a problem in handling very low-n modes and simulation domains are still limited to annular wedge torus domain.

To simulate tokamak edge MHD/turbulence in full annular torus domain, a novel hybrid Poisson solver consisting of a flute-ordering-free Poisson solver designed for n=0 and low-n modes and the conventional flute-ordered Poisson solver for moderate-n and high-n mode is developed. The numerical detail of the hybrid Poisson solver is left for future publications.

The hybrid Poisson solver is tested with a simulation of ELM crash triggered by resistive ballooning mode (RBM) and drift wave (DW) instabilities in a full annular torus domain with shifted circular cross section. Here the simulation setup including the governing equations and the equilibrium but the grid resolution and the toroidal domain length is same as is reported in Ref [11]. For the computational domain, the radial grid number is 512 for $0.6 \leq x \leq 1.2$, the parallel grid number is 128 for $0 \leq y \leq 2\pi$ and the binormal grid number is 256 for $0 \leq z \leq 2\pi$ respectively. For the hybrid Poisson solver, the flute-ordering-free Poisson solver is applied from n=0 to n=4 modes, and the flute-ordered Poisson solver is applied from n=5 to n=80 modes and n>80 modes are numerically removed respectively.

Figure 1 shows the dispersion relation of initially unstable modes where n=32 is the most unstable mode in this simulation, and Fig. 2 also shows the time evolution of perpendicular kinetic energy spectra with respect to toroidal mode number

respectively. In this simulation, the large energy loss by ELM driven by RBM and DW occurs at t~250t_A.

The time evolution of perpendicular kinetic energy spectra shows that the initially unstable modes get saturated at t~150t_A and the very low-n modes (n=1~3) are then driven in prior to the zonal mode (n=0) via nonlinear couplings among initially unstable modes as is shown in Fig.2(b) and Fig. 2(c). After the saturation of very low-n modes and zonal mode, the large pedestal collapse triggered by the initially unstable high-n modes (n~32) and the moderate-n modes (n~20) in Fig. 2(d), and the zonal mode becomes dominant after the pedestal collapse in Fig. 2(e). This multi-phase collapse is not observed in our previous works [10, 11] using 1/5th annular wedge torus domain due to lack of very low-n modes.

In summary, the hybrid Poisson solver has been developed for full annular tokamak edge simulation in BOUT++ framework. It has been demonstrated that the usage of full annular torus domain can change the dynamics of ELM driven by high-n RBM and DW modes. The detailed analyses such as energy transfer among toroidal modes, the spatial structure of low-n modes, are left as future works.

Acknowledgements:

This work was partially supported by JSPS KAKENHI Grant No. 20K14448 and performed under EU-Japan BA collaboration, under JIFT collaboration between QST and LLNL and under the auspices of the U.S. Department of Energy by LLNL under Contract No. DE-AC52-07NA27344. Computations were carried out on JFRS-1 supercomputer at International Fusion Energy Research Centre Computational Science Cenre (IFERC-CSC) and on HPE SGI8600 supercomputer at QST and JAEA.

References:

[1] H. Zohm, Plasma Phys. Control. Fusion **28**, (1996) 1213
[2] J.P. Gunn et al. Nucl. Fusion **57**, (2017) 046025
[3] C.F. Maggi et al., Nucl. Fusion **55**, (2015) 113031
[4] G.S. Xu et al., Phys. Rev. Lett. **112**, (2019) 255001
[5] N. Oyama et al., Nucl. Fusion **50**, (2010) 064014
[6] B.D. Dudson et al., Comput. Phys. Commun. **180** (2009) 1467
[7] M.A. Beer et al., Phys. Plasmas **2**, (1995) 2687
[8] X.Q. Xu et al., Phys. Rev. Lett. **105** (2010) 175005
[9] B.D. Dudson and J. Leddy, Plasma Phys. Control. Fusion **59** (2017) 054010
[10] H. Seto et al., Phys. Plasmas **26** (2019) 052507
[11] H. Seto et al., Contrib. Plasmas Phys. **60** (2020) e201900158

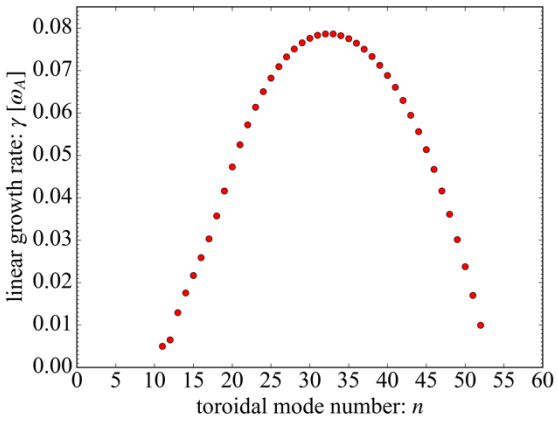

Fig. 1: dispersion relation of initially unstable RBM+DW instability, where the most instable mode is n=32

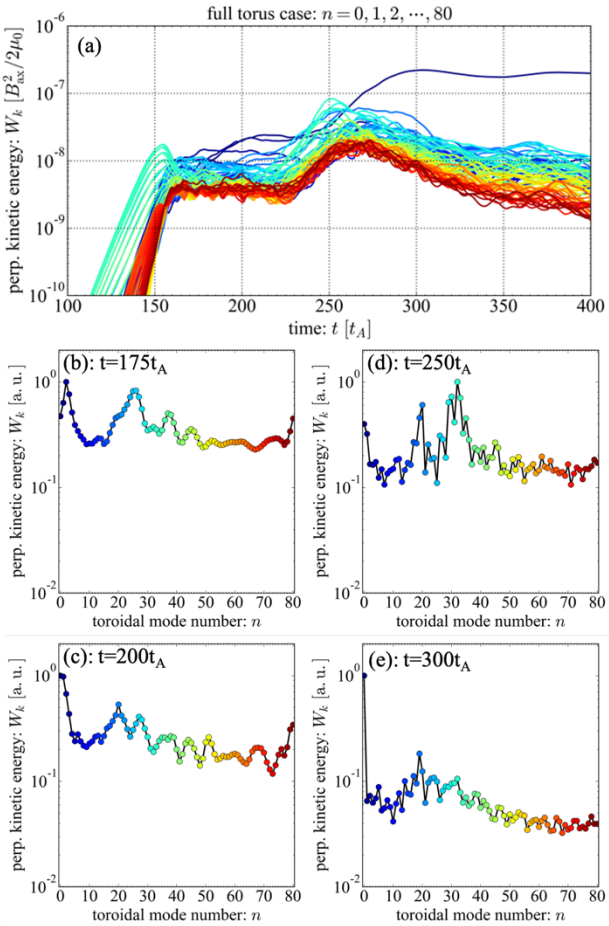

Fig. 2: (a) time evolution of perpendicular kinetic energy spectra and time slices of normalized perpendicular kinetic energy spectra at four time slices, where (b) and (c) are in nonlinear phase before the pedestal collapse, (d) is during the pedestal collapse and (e) is after the pedestal collapse respectively.

Prediction of turbulence temporal evolution in PANTA by Long-short term memory network

College of Industrial Technology, Nihon University
M.Aizawa Caranza, M.Sasaki, H.Minagawa, Y.Nakazawa, Y.Liu, Y.jazima, K.Hara

1. Introduction

The prediction of the plasma behavior including turbulence is an urgent issue for the dynamic control of the magnetic confinement plasma. In this study, we perform time series prediction using LSTM for multi-scale turbulent time series observed by Langmuir probes in the linearly magnetized plasma experimental device PANTA, and describe the prediction characteristics when the training conditions of the networks are varied.

2. Prediction Method・Evaluation Method

LSTM (Long-short term memory) is a kind of recurrent neural network[1], which is suitable for time series forecasting of multi-scale fluctuations because it can learn while retaining past information. The LSTM has the network structure shown in Fig. 1, with multiple units called LSTM Blocks in the middle layer, cells that store past information in the units, and three gates (input gate, forget gate, and output gate) that control the flow of information. By adjusting the degree of flow of this gate, storing it in a cell, and inputting the information from the output and the intermediate layer unit into the next intermediate layer, it is possible to learn based on past information.

In this study, Prediction of plasma turbulence using the waveform of ion saturation current in turbulent plasma measured by PANTA. This turbulence data is, Short-period drift-wave turbulence is dominant, and long-period abrupt transport is driven by its nonlinear processes [2]. The prediction of long-period abrupt transport is an important technique for the control and operation of fusion plasmas.

We used 80% of the first half of the turbulent time series as training data and 20% of the second half for prediction (see Fig. 2). For the evaluation of the learning efficiency, the cross spectrum evaluated from the predicted and observed values was used to examine the prediction accuracy.

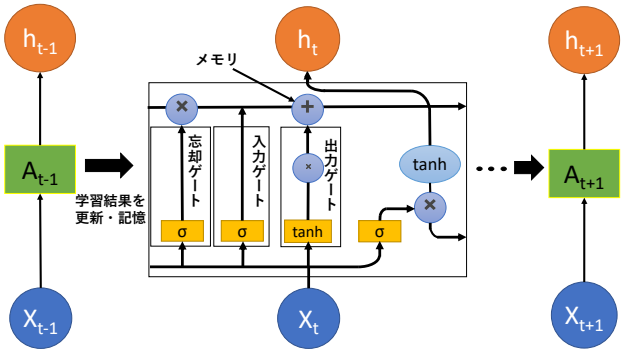

Fig. 1 Structure of the LSTM to be used

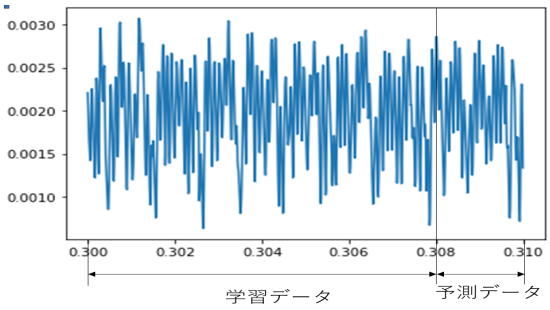

Fig. 2 Range of training and prediction

3.Result

In the case of normal prediction using LSTM, the dominant drift wave frequency band of this turbulence data is about 10 kHz, and the dominant frequency components could be predicted, but it was difficult to improve the prediction accuracy for low-frequency components of about 5 kHz. Since the prediction of the low-frequency component, which corresponds to nonlinear abrupt transport, is intrinsically important, the high-frequency component and the averaged

component were removed from the prediction. By narrowing down the target frequency, we succeeded in improving the prediction accuracy of the low-frequency component, as shown in Fig. 3.

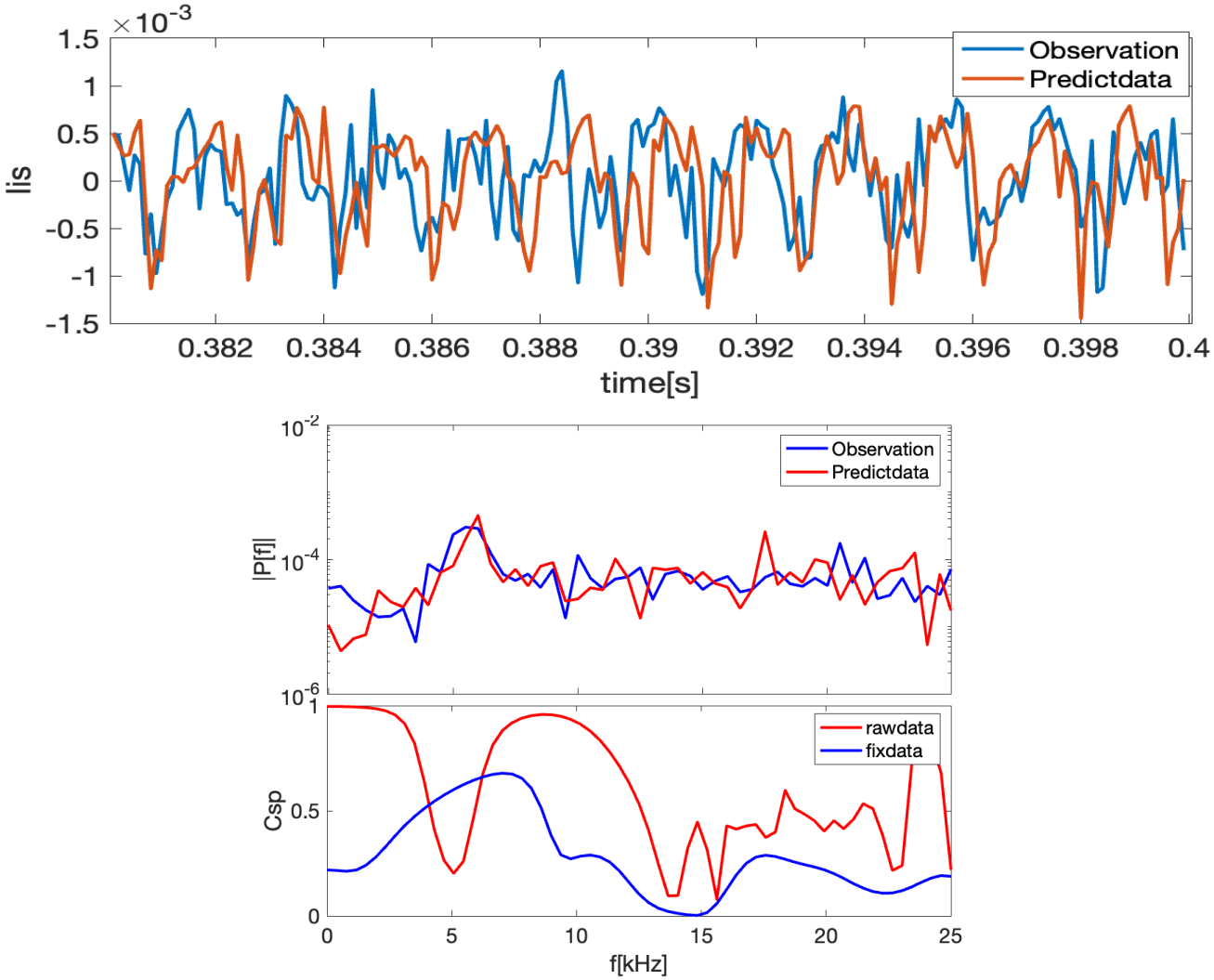

Fig. 3 Prediction results when high frequency components are excluded.
(Top: Comparison of predicted and observed values, Bottom: Spectrum and cross spectrum of both)

4.Summary

Time series prediction of plasma turbulence as a typical multiscale fluctuation is carried out using LSTM network and the prediction characteristics are clarified. It is found that the prediction of dominant coherent fluctuations is possible, and that the performance of the prediction of low-frequency fluctuations can be improved by removing the high-frequency and averaged components.

REFERENCE

[1] Sepp Hochreiter, Jürgen Schmidhuber (1997) ”LONG SHORT-TERM MEMORY”, Neural Computation **9** (8): 1735–1780.

[2] F. Kin, Phys. Plasmas,**26**, 042306 (2019)

Analysis of three-dimensional structure of MHD instabilities in tokamak

Y. Kuroda[1], N. Kasuya [1,2], M. Sato [3], M. Sasaki [4]

IGSES, Kyushu Univ. [1], RIAM, Kyushu Univ.[2], NIFS[3], CIT, Nihon Univ.[4]

1. Introduction

In tokamak devices, Magneto-Hydro-Dynamics (MHD) instabilities is induced by large pressure gradient and plasma current, which cause confinement degradation and plasma collapse. Therefore, it is essential to evaluate their excitation and saturation mechanisms. Numerical simulations give three-dimensional (3-D) structures of the plasma instabilities for comparison with experimental measurements [1].

In a previous study [2], simulations of MHD instability have been performed for the tokamak device PLATO [3]. From the simulation results, ballooning instability and kink instability both can be excited and the characteristics of the instabilities with different safety factor profiles have been evaluated.

In this study, under the condition when several characteristic instabilities are excited, we extract their characteristic structures by Fourier mode decomposition, and dynamic mode decomposition (DMD), which has recently been used for dynamic structure extraction.

2. Simulation code

In this study, MHD simulations are carried out for tokamak device PLATO by using MIPS code [4]. Since the simulation requires initial equilibrium data, this routine uses TASK/EQU [5], which allows equilibrium calculation under free boundary conditions including the fields induced by the external coil current in the experimental condition. The equilibrium obtained in the calculation is introduced into the MHD simulation code MIPS to perform a three-dimensional simulation of the MHD instability. The expected plasma parameters of PLATO tokamak are the followings; major radius $R = 0.7\ m$, minor radius $a = 0.2\ m$, plasma volume $V_P = 0.9\ m^3$, electron temperature $T_e = 0.2\ keV$, density $n = 1.0 \times 10^{19}\ m^3$.

3. Analysis method

In a previous study, the mode spectrum analysis was performed using Fourier expansion. Fourier mode expansion decomposes a waveform into periodic sine and cosine waves with different amplitudes, frequencies, and phases. However, it is difficult to evaluate the characteristic mode structure in Fourier transform when there exists frequency temporal variation or spatial localization. Therefore, mode spectrum analysis is carried out using DMD. DMD focuses on the time evolution of time series data for performing mode decomposition, Characteristic modes and their corresponding frequencies can be obtained.

4. MHD simulation result

The MHD simulations are carried out under the condition that both ballooning and kink modes are excited. The used plasma parameters are as follows; central safety factor $q_0 = 0.8$, central beta value $\beta_0 = 1.5$, viscosity $\nu = 10^{-5}$, resistibility $\eta = 10^{-5}$, thermal diffusion coefficient $\chi = 10^{-7}$. Figure 1 shows time evolution of the pressure profile. In Fig.1(b), a ballooning mode structure whose perturbation component exists in the low field side of torus plasma can be seen with finite poloidal mode numbers. The ballooning

mode consists of multiple Fourier modes with poloidal mode number m = 14 - 25 as shown in Fig. 2. In Fig.1(c), a kink mode structure exists near the plasma center. In this way, both of ballooning and kink modes are excited in this simulation.

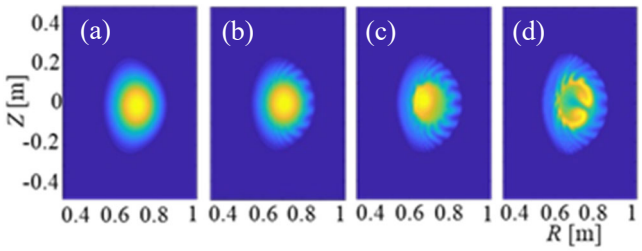

Fig.1 Time evolution of the pressure profile in the poloidal cross-section (t = (a) 0, (b) 350, (c) 460, (d) 500)

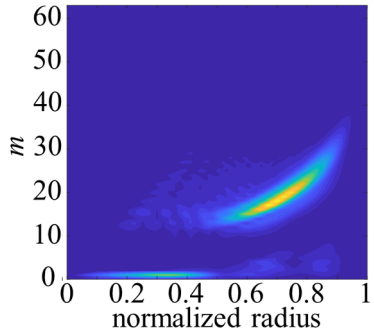

Fig.2 Radial profiles of the mode spectrum (t = 350)

5. Fourier mode expansion result

Next, dynamics of the modes is analyzed with the time evolution of Fourier modes. Figure 3 shows the radial profiles of Fourier modes when the (a) ballooning and (b) kink mode are excited. The kink mode component is excited near the center of the plasma and propagates to the outer region. In Fig.3(b), the kink mode reaches the position where the ballooning mode exists. Then the kink mode is weakened, and propagates to the outer region with reduction of the amplitude. When the ballooning mode is not excited, the kink mode directly propagates to the outer region without amplitude reduction (Fig. 3(c)). The mitigation of the mode propagation occurs near the rational surface q = 1 in this case, but there is no qualitative change with the variation of the q profile. Therefore, the magnetic configuration is not the cause of this phenomenon.

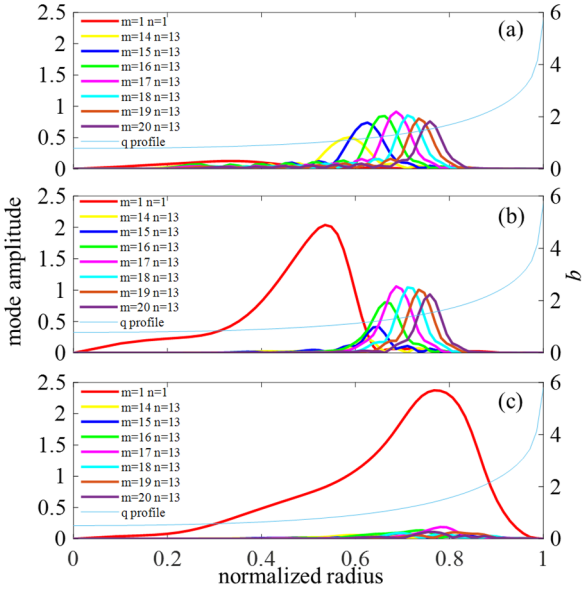

Fig.3 Radial profiles of the Fourier components at t = (a) 350 (only ballooning mode is dominant) and (b) 490 (competition between the ballooning and kink modes) with q_0 = 0.8. The case only with a kink mode by changing the q profile with q_0 = 0.5 is also shown in (c).

Mode coupling between the kink and ballooning modes is the candidate. To confirm this, time evolutions of the mode components are evaluated. When the kink mode reaches at the edge of the ballooning mode region $\rho \sim 0.5$, the amplitude of the ballooning mode begins to be reduced, compared with the case without the ballooning mode. This is related to flattening of the background plasma profile due to the ballooning mode (quasi-linear effect). On the other hand, the time evolution of the ballooning mode amplitude has bump, when the kink component reaches that position $\rho \sim 0.7$. This might be the appearance of the energy transfer from the kink to the ballooning mode. It is suggested that the interaction between the components affects the propagation.

6. Dynamic mode decomposition result

Next, DMD is applied to analyze the mode structure [6]. By using DMD, it is possible to extract the whole image of the characteristic structure, which is expressed as the addition of many modes in Fourier mode. Figure 4 shows the example of DMD mode in the time evolution of the MHD instabilities. In Fig.4, the high wavenumber component and the kink component were extracted. Since the growth rates of the high wave number component and the kink mode component are comparable, mixed structures of them were extracted as the DMD modes. Figure 5 shows reconstruction of the time series of the pressure profile from the decomposition modes. Figure 5(a)and (b) is the reconstruction from a few number of modes and the original data, respectively. From these results, it is possible to reproduce the characteristics with a limited number of DMD modes.

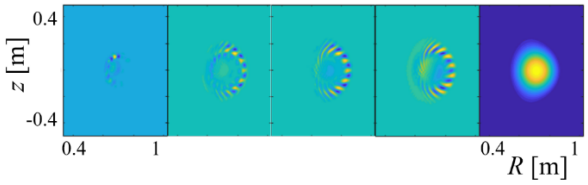

Fig.4 The example of DMD mode (localized mode, ballooning mode, mixture of ballooning and kink mode, mean profile)

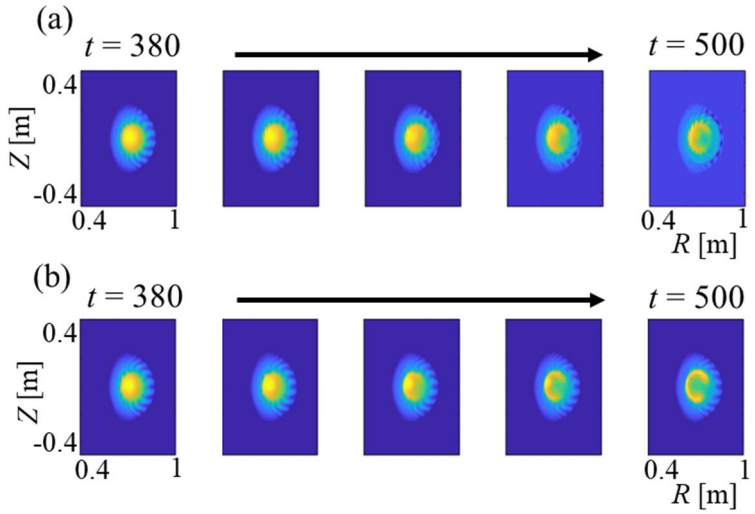

Fig.5 (a) Reconstruction of time series of pressure profile from a few number of modes, and original data.

7. Conclusion and future plan

In this study, 3-D simulation of MHD instabilities were carried out for the PLATO device. Fourier mode expansion analysis and dynamic mode decomposition for the perturbation mode structure was carried out in the time evolution of competition between ballooning and kink instabilities. Interpretation of mode structures extracted by dynamic mode decomposition and quantitative evaluation of interaction between modes will be the future task.

References

[1] C. Holland, *et al*, Phys. Plasmas **16** (2009) 052301.

[2] S. Tomimatsu, *et al*, Plasma Fusion Res. **15** (2020) 1403052.

[3] A. Fujisawa, AIP Conf. Proc. **1993** (2018) 020011.

[4] Y. Todo, *et al*, Plasma Fusion Res. **5** (2010) S2062.

[5] http://bpsi.nucleng.kyoto-u.ac.jp/task/

[6] M. Sasaki, *et al*, Plasma Phys. Control. Fusion **61** (2019) 112001.

Prediction of temperature profiles in helical plasmas by integrated code coupled with gyrokinetic transport models

S. Toda, M. Nunami, and H. Sugama

National Institute for Fusion Science, Oroshi-cho 322-6, Toki, Gifu, 509-5292, Japan

To realize fusion energy, prediction of turbulent transport in toroidal plasmas is one of the most critical issues to be solved. Study of zonal flow effects on plasma confinement improvement is necessary for accurate prediction of turbulent transport and plasma profiles. A large number of gyrokinetic turbulence transport simulations have been performed for tokamak plasmas and for helical plasmas [1, 2, 3]. In tokamak plasmas, transport simulation, which is coupled to gyrokinetic analysis results, is performed. Much larger computer resources are consumed to perform gyrokinetic simulation in helical plasmas than in tokamak plasmas, because the former requires a large number of mesh points along field lines to resolve helical ripple structures. Since combining nonlinear gyrokinetic simulation with integrated simulation in helical plasmas is not yet easy, there is a strong need for predictive models which can quickly reproduce nonlinear simulation results. Heat diffusivity models for electron and ion heat transport, and quasilinear flux models for particle and heat transport have been proposed in a kinetic electron condition for ion temperature gradient (ITG) turbulence in the Large Helical Device (LHD) [2]. The nonlinear simulation results are quickly evaluated by reduced models, because these models are basically functions of the quantity related with a linear growth rate and the characteristic quantity for linear response of zonal flows (the zonal flow decay time [4]). The heat diffusivity models have been installed into transport code for simulating evolutions of the plasma profiles in the LHD when additional modeling by normalized ion temperature scale length is used [5, 6]. Since the density gradient which is necessary to construct an effective diffusivity model is not accurately evaluated for the hollow and flattened density profiles which are typical in LHD experimental results, particle diffusivity is hard to be modeled. Furthermore, dynamical transport simulation with a quasilinear flux model installed has not been performed so far, because the quasilinear flux model depends on a cross-phase between fluctuating potential and temperature (or density) and this cross-phase term is difficult to be modeled by temperature or density gradients. The quasilinear flux formulation enables us to model particle and heat transport for flattened or hollow density and temperature profiles. The nonlinear simulation results can be predicted by the reduced models for the ion heat transport [3]. The simulation which includes multi-time scales is a challenging task, because the difference between energy confinement time (around 1s) and a typical gyrokinetic time scale (around 1μs) is extremely large. To obtain the temperature profiles, the transport simulation with the gyrokinetic transport models installed is performed by the integrated code in this article, where the heat diffusivity and quasilinear flux models are evaluated by the linear gyrokinetic simulation by GKV code [7] at each time step in the evolution of the integrated simulation. The zonal flow decay time is fixed in the transport simulation. The linear simulations are performed for the various temperature profiles to evaluate the reduced transport models at each time step in the integrated simulation.

The reduced turbulent transport model is evaluated by the linear gyrokinetic simulation using local flux tube code, GKV. The integrated simulation is performed by the TASK3D code. In the integrated simulation by TASK3D, the heat transport consists of turbulent and neoclassical parts. The neoclassical diffusion coefficient is derived from the DGN/LHD database. The turbulent transport is evaluated by the reduced models. The linear growth rates are evaluated at $t_{\rm g} = 50R/v_{\rm ti}$ in the linear gyrokinetic simulation at an equally spaced twenty radial points in the region $0.0 < \rho < 0.8$. Here, $\rho = r/a$, $t_{\rm g}$ is the time period treated in the linear gyrokinetic simulation, $\tilde{k}_x$ is the normalized radial wavenumber, r is the radial coordinate and a is the minor radius. The flux tubes of the GKV code are set at each radial point. The value of $50R/v_{\rm ti}$ is typically $\simeq 10^{-5}$s in the plasma parameter region studied here. The integrated simulation by the TASK3D is performed at the eighty radial points in the region $0.0 < \rho < 0.8$, where the time step in the integrated simulation, dt is set to 10^{-3}s. The quantities $\mathcal{L}$ related with the mixing length estimate at the sixty radial points, where the gyrokinetic simulation is not done, are interpolated from those which are calculated by the GKV at the equally spaced twenty radial points. The value of the linear growth rate is determined once one cycle of the integrated simulation is performed. The time of $50R/v_{\rm ti}(\simeq 10^{-5}$s) for the gyrokinetic simulation is one hundredth of $dt(= 10^{-3}$s) in the integrated simulation using the TASK3D. The results of the temperature profile for one cycle of the integrated simulation are used as initial conditions for the next cycle. The cycle of the integrated simulation is repeated twenty times until the temperature profiles become stationary in the parameter region studied here.

The transport simulation is performed by the integrated code using the reduced gyrokinetic models. Especially, the quasilinear flux model is used in helical plasmas. The turbulent transport is evaluated by reduced models using the linear gyrokinetic simulation results for the kinetic electron response at each time step in the integrated simulation. By performing the integrated simulation with the gyrokinetic models installed, multi-time scale simulation can be performed. The multi-time scale simulation is done for the high-$T_{\rm i}$ plasmas in the standard field configuration and the low-$T_{\rm i}$ plasmas in the inward shifted field configuration of the LHD. The stationary temperature profiles predicted by the transport simulation, using the reduced models which reproduce the nonlinear simulation results, are predicted within a difference of 30% at most from the experimental results in the LHD, where the ITG mode is unstable. The simulation using the quasilinear flux model, including effects of zonal flows and kinetic electrons, is performed for the first time to predict the temperature profiles in the LHD. This is achieved by combining the two codes, TASK3D and GKV, developed for helical plasmas. How to construct the models [1, 2] by linear simulation results is applicable to other plasmas in helical devices where modes other than the ITG mode are unstable, and to plasmas in tokamak devices by capturing the dependence of turbulent transport on the linear properties in the reduced models. By these reduced models, the integrated simulation with the gyrokinetic model installed will be performed to predict plasma profiles and confinement properties. This is left for future studies.

This work is partly supported by the NIFS Collaboration Research Programs, NIFS20KNST168

(Plasma Simulator), the JSPS KAKENHI Grant No. 21K03514 and the Collaborative Research Program of Research Institute for Applied Mechanics, Kyushu University, 2021FP-06.

[1] M. Nunami *et al.*, *Phys. Plasmas* **20** 092307 (2013)

[2] S. Toda *et al.*, *Phys. Plasmas* **26** 012510 (2019)

[3] S. Toda *et al.*, *J. Plasma Phys.* **86** 815860304 (2020)

[4] H. Sugama and T. -H. Watanabe, *Phys. Plasmas* **13** 012501 (2006)

[5] S. Toda *et al.*, *J. Phys. Conf. Ser.* **561** 012020 (2014)

[6] S. Toda *et al.*, *Plasma and Fusion Research* **14** 3403061 (2019)

[7] T. -H. Watanabe and H. Sugama, *Nucl. Fusion* **46** 24 (2006)

トーラスプラズマにおける 3 次元データを用いた揺動計測模擬

Numerical diagnostics of plasma fluctuations by using 3-D simulation data in torus plasmas

N. Kasuya[1,2], R. Yoshihara[2], T. Ido[1,2], Y. Kuroda[2], M. Yagi[3], M. Nunami[4], Y. Nagashima[1,2], A. Fujisawa[1,2]
[1] RIAM, Kyushu University, Kasuga, Fukuoka 816-8580, Japan
[2] IGSES, Kyushu University, Kasuga, Fukuoka 816-8580, Japan
[3] QST, Obuchi, Rokkasho, Aomori 039-3212, Japan
[4] NIFS, Toki, Gifu 509-5292, Japan
E-mail: kasuya@riam.kyushu-u.ac.jp

Plasma turbulence largely affects particle and heat transport in torus plasmas, so it is important to clarify its 3-D feature by detailed measurements in experiments. Synthetic diagnostics uses simulation data to represent experimental measurements and to make quantitative evaluations [1]. Simulations can show global features of plasma fluctuations, and quantitative comparison between experiments and simulations is possible by simulating measurement signals numerically using simulation data. Simulation models are different each other, depending on each simulation target, so comparison between models is also important to capture various characteristics in magnetized plasmas. We are now developing integrated numerical diagnostic platform, which can be applied to multiple simulation data that have different data formats [2]. Three kinds of perturbation data are analyzed with a numerical heavy ion beam probe (HIBP) routine. The construction of the developed routines and calculation results using them are described in this presentation.

Heavy ions with 1+ charge is injected into a core plasma and are ionized to 2+ charge ions by collision. By measuring the energy of the ionized ions, HIBP observes the potential, density and magnetic field at a local point in core plasma [3]. PLATO tokamak device [4] is now constructed to begin the detailed plasma turbulence observation [4]. Multiple HIBPs will be installed in PLATO for simultaneous measurement at different poloidal and toroidal positions. For numerical HIBP, 3-D potential, density and temperature profiles are necessary. Mean on the magnetic flux surface and perturbation quantities with 3-D variations make possible to carry out a simulation of fluctuation measurement. Constant temperature is assumed for simplicity in this time, so the spatial variation of the collisional cross section is not considered. Here 3-D profiles obtained from MIPS [5]、R4F [6]、FORTEC-3D [7] are analyzed. All of them are the calculation results in torus plasmas. In general, particular models do not always include all the necessary quantities, so insufficient ones are supplemented with any assumptions. In addition, spatial coordinates may be different, so data transfer to the coordinates for the numerical measurement is necessary. Data mapping to the common format is often used, but here we introduce the object-oriented method in accordance with each data format to gain the maximum information. MIPS is the 3-D MHD code, which

provides 3-D data in torus meshes with same intervals. A MHD small collapse driven by pressure gradient is analyzed by using MIPS. R4F is the 4-field reduced MHD code, which provides 1-D differential data in the radial direction and 2-D spectral expansion data in the poloidal and toroidal directions. Global MHD mode and micro turbulence are analyzed by using R4F. FORTEC-3D is the drift-kinetic code, which provides profile data in the flux surface coordinates for the analyses. Inhomogeneous potential on the flux surfaces is analyzed from neoclassical transport in helical plasmas by using FORTEC-3D.

[1] C. Holland, *et al.*, Phys. Plasmas **16** (2009) 052301.
[2] N. Kasuya, *et al.*, 28th Int. Toki Conf. (Toki, Gifu, 2019) P2-01.
[3] T. Ido, *et al.*, Rev. Sci. Instrum. **77** (2006) 10F523.
[4] A. Fujisawa, AIP Conf. Proc. **1993** (2018) 020011.
[5] S. Tomimatsu, *et al.*, Plasma Fusion Res. **15** (2020) 1403052.
[6] M. Yagi, *et al.*, Plasma Fusion Res. **2** (2007) 025.
[7] S. Satake, *et al.*, Plasma Fusion Res. **3** (2008) S1062.

Development of a semi-empirical particle and heat transport model and improvement in its turbulent saturation rule

E. Narita[1], M. Honda[2], M. Nakata[3,4], M. Yoshida[1] and N. Hayashi[1]

[1]National Institutes for Quantum Science and Technology, Naka, Ibaraki 311-0193, Japan

[2]Graduate School of Engineering, Kyoto University, Nishikyo, Kyoto 615-8530, Japan

[3]National Institute for Fusion Science, Toki, Gifu 509-5292, Japan

[4]The Graduate University for Advanced Studies, Toki, Gifu 509-5292, Japan

1 Introduction

The gyrokinetic-based turbulent transport models, such as TGLF [1,2], are essential to predict density and temperature profiles, but introducing detailed descriptions of turbulence physics tends to increase the computational cost. To accelerate the profile predictions, a neural-network (NN) based approach has been undertaken (see e.g., [3–6]). Our study is also developing a NN-based turbulent transport model DeKANIS [7,8]. A turbulent saturation rule employed in DeKANIS was based on experimental particle fluxes estimated for JT-60U H-mode plasmas, and it was apt to overestimate temperatures. To reduce the overestimation, a different saturation rule is built including experimental heat fluxes.

2 Transport model DeKANIS and its original saturation rule

DeKANIS predicts turbulent particle and heat fluxes for electrons in a quasilinear limit as $\bar{\Gamma}_\mathrm{e} = \bar{D}\left(\frac{R}{L_{n_\mathrm{e}}} + C_\mathrm{T}\frac{R}{L_{T_\mathrm{e}}} + C_\mathrm{P}\right)$ and $\bar{Q}_\mathrm{e} = \bar{\chi}_\mathrm{e}\left(C_\mathrm{N}\frac{R}{L_{n_\mathrm{e}}} + \frac{R}{L_{T_\mathrm{e}}} + C_\mathrm{HP}\right)$, respectively. Here, non-dimensional $\bar{D}$, $\bar{\chi}$, R/L_n and R/L_T are the particle and heat diffusivities in proportion to fluctuation amplitudes and the density and temperature gradients, respectively. The fluxes are composed of the diagonal (diffusive) and off-diagonal (non-diffusive) terms, which are quantitatively determined by calculating the off-diagonal-term coefficients ($C_\mathrm{T,P,N,HP}$) and the diffusivities ($\bar{D}$ and $\bar{\chi}_\mathrm{e}$). Note that as the first off-diagonal terms of $\bar{\Gamma}_\mathrm{e}$ and $\bar{Q}_\mathrm{e}$ satisfy the Onsager symmetry, the following relationship is obtained: $\bar{\chi}_\mathrm{e} = \bar{D}(C_\mathrm{T} + 1.5)/C_\mathrm{N}$. Predicting diagonal and off-diagonal terms individually could be helpful to understand the effects of the transport processes on density and temperature profile formation. In addition to the electron fluxes, DeKANIS predicts the ion heat flux, which is given as $\bar{Q}_\mathrm{i} = \frac{\bar{\chi}_\mathrm{i,eff}}{\bar{\chi}_\mathrm{e,eff}}\bar{\chi}_\mathrm{e,eff}\frac{R}{L_{T_\mathrm{i}}}\frac{n_\mathrm{i}}{n_\mathrm{e}}\frac{T_\mathrm{i}}{T_\mathrm{e}}$. Here, $\bar{\chi}_\mathrm{eff}$ is the normalized effective heat diffusivity, which is defined when the heat flux is expressed with only the diagonal term. Once $\bar{\chi}_\mathrm{e,eff}$ is obtained with $\bar{Q}_\mathrm{e}$, $\bar{Q}_\mathrm{i}$ can be constructed through $\bar{\chi}_\mathrm{i,eff}/\bar{\chi}_\mathrm{e,eff}$.

DeKANIS estimates $C_\mathrm{T,P,N,HP}$, $\bar{D}$, $\bar{\chi}_\mathrm{e}$ and $\bar{\chi}_\mathrm{e,eff}/\bar{\chi}_\mathrm{i,eff}$ with a NN model. The training dataset has been developed based on 23 JT-60U H-mode plasmas. Turbulence of these plasmas is dominantly driven by the ion temperature gradient (ITG) mode or the ITG/trapped electron mode. In the dataset, $C_\mathrm{T,P,N,HP}$ and $\bar{\chi}_\mathrm{e,eff}/\bar{\chi}_\mathrm{i,eff}$ are given by linear gyrokinetic calculations with GKW [9]. On the other hand, $\bar{D}$ has been determined by the two different saturation rules. The first rule, the semi-empirical saturation rule, calculates $\bar{D}$ to match it to the the experimental

Table 1. The exponents α and β and proportionality constant c of the scaling formulas.

Base	α	β	c $[10^{-4}]$
$\bar{\Gamma}^{\rm exp}_{\rm e,turb}$	1.1008	−2.8024	1.6996
$\bar{Q}^{\rm exp}_{\rm e,turb}$	1.1990	−2.4732	7.8584

turbulent particle flux $\bar{\Gamma}^{\rm exp}_{\rm e,turb}$. The second rule will be shown in later. The output parameters of the NN model are $C_{\rm T,P,N,HP}$, $\bar{D}$ and $\bar{\chi}_{\rm e,eff}/\bar{\chi}_{\rm i,eff}$, and with the coefficients, $\bar{\chi}_{\rm e}$ is computed not to break the Onsager symmetry.

When DeKANIS is applied to predicting particle and heat fluxes of 14 JT-60U H-mode plasmas that are not used for the training dataset, $\bar{Q}_{\rm e}$ and $\bar{Q}_{\rm i}$ tend to be underestimated in $\rho > 0.3$ by comparison with $\bar{\Gamma}_{\rm e}$ as shown with the mean offset (MOFF) in figure 1(a), where ρ is the normalized minor radius. Here, MOFF of an arbitrary ξ is defined as MOFF $= (1/N)\sum(\xi_{\rm DeKANIS}/\xi_{\rm exp} - 1)$. Because of the underestimate, $T_{\rm e}$ and $T_{\rm i}$ are overestimated when the density and temperature profiles are predicted with the integrated code TOPICS [11], as shown in figure 1(b). The overestimated temperatures accompanied by steeper temperature gradients cause an increase in the particle flux through the off-diagonal terms. Since the value of the diagonal term of the particle flux needs to decrease to offset the increase in that of the off-diagonal ones, the density profile tends to be flat, yielding an underestimate of the density.

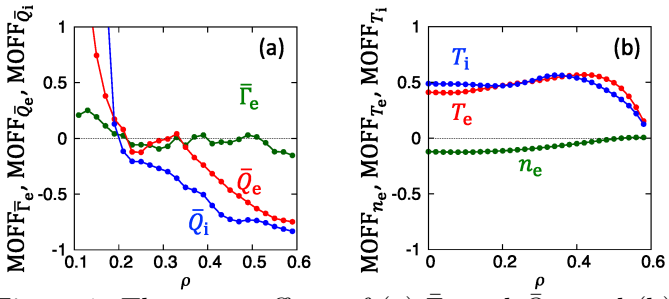

Figure 1. The mean offsets of (a) $\bar{\Gamma}_{\rm e}$ and $\bar{Q}_{\rm e,i}$ and (b) $n_{\rm e}$ and $T_{\rm e,i}$ predicted with the semi-empirical saturation rule for 14 JT-60U test cases at each radial point.

3 Mixing-length-like saturation rules

The second saturation rule is based on the mixing-length theory, assuming that $\bar{D}$ is expressed by the quasilinear diffusivity $\bar{\gamma}/\bar{k}_\theta^2$ characterizing instabilities and the residual zonal flow level $\mathcal{L}_{\rm ZF}$ [12]: $\bar{D} = c\,(\bar{\gamma}/\bar{k}_\theta^2)^\alpha\,\mathcal{L}_{\rm ZF}^\beta$. Here, $\mathcal{L}_{\rm ZF}$ is defined as $\mathcal{L}_{\rm ZF} \equiv \mathcal{K}_{\rm RH}\,(\bar{\gamma}/\bar{k}_\theta^2)^{0.5}$, where $\mathcal{K}_{\rm RH} = 1/(1+1.6q^2/\epsilon^{1/2})$ with the safety factor q and the inverse aspect ratio ϵ [13]. When the mixing-length-like saturation rule is used, yet another NN model is applied, which forecasts the maximum linear growth rate $\bar{\gamma}_{\rm max}$ and the wavenumber k_θ with $\bar{\gamma}_{\rm max}$ based on the GKW calculations. $\bar{D}$ is computed by using $\bar{\gamma}_{\rm max}$ and k_θ given by the NN model with the scaling formula. The exponents α and β and proportionality constant c of the original scaling formula were derived from a manual regression analysis for $\bar{D}$ evaluated based on $\bar{\Gamma}^{\rm exp}_{\rm e,turb}$ in the same manner as the semi-empirical saturation rule. In this paper, the regression analysis is performed for $\bar{D}$ estimated to match it to the experimental electron turbulent heat flux $\bar{Q}^{\rm exp}_{\rm e,turb}$. Also, α, β and c are optimized with a genetic algorithm. To check the effect of the change in the basic experimental value, the scaling formula optimized for $\bar{\Gamma}^{\rm exp}_{\rm e,turb}$ is also created.

The obtained two scaling formulas based on $\bar{\Gamma}^{\rm exp}_{\rm e,turb}$ and $\bar{Q}^{\rm exp}_{\rm e,turb}$ have α, β and c shown in table 1. Since the two scaling formulas share comparable α and β, they show similar effects of instabilities and zonal flows. On the other hand, c increases if the basic experimental value is

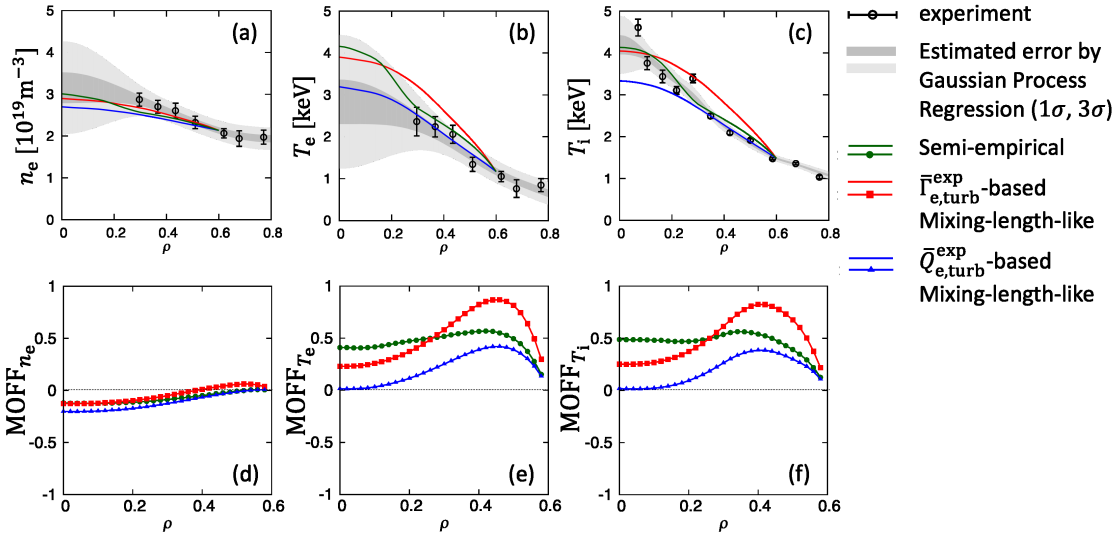

Figure 2. Radial profiles of (a) n_e, (b) T_e and (c) T_i predicted with the semi-empirical saturation rule and the two mixing-length-like saturation rules for a JT-60U plasma outside the training dataset. The mean offsets of (d) n_e, (e) T_e and (f) T_i predicted with the three saturation rules for 14 JT-60U test cases at each radial point.

$\bar{Q}^{exp}_{e,turb}$. When these formulas are used in TOPICS, due to the larger c, the $\bar{Q}^{exp}_{e,turb}$-based mixing-length-like saturation rule predicts lower temperatures as shown in figure 2(b) and (c) with the larger heat fluxes in comparison with the semi-empirical saturation rule and the $\bar{\Gamma}^{exp}_{e,turb}$-based mixing-length-like one. As for the density profile, the three saturation rules gives similar results (figure 2(c)). The tendencies are also observed in the MOFF profiles for the 14 JT-60U H-mode plasmas outside of the training and regression datasets as shown in figure 2(d)–(f). One can find that the temperature overestimation is reduced by introducing $\bar{Q}^{exp}_{e,turb}$ in the saturation rule.

Further improvement in the saturation rule is, however, required, because the current scaling formulas show weak dependence of $\bar{D}$ on $\bar{\gamma}/\bar{k}^2_\theta$ as $\alpha \sim -0.5\beta$. It contradicts the well-known mixing-length rule. Furthermore, we need to investigate the nature of the inconsistency of c between the two scaling formulas, since the inconsistency indicates that $\bar{Q}_e/\bar{\Gamma}_e$ estimated by the quasilinear theory does not match the experimental value.

References

[1] G.M. Staebler *et al.,* Phys. Plasmas **12** 102508 (2005).
[2] G.M. Staebler *et al.,* Nucl. Fusion **61** 116007 (2021).
[3] M. Honda and E. Narita, Phys. Plasmas **26** 102307 (2019).
[4] M. Honda and E. Narita, Plasma Fusion Res. **16** 2403002 (2021).
[5] O. Meneghini *et al.,* Nucl. Fusion **61** 026006 (2021).
[6] K.L. van de Plassche *et al.,* Phys. Plasmas **27** 022310 (2020).
[7] E. Narita *et al.,* Nucl. Fusion **59** 106018 (2019).
[8] E. Narita *et al.,* Nucl. Fusion **61** 116041 (2021).
[9] A.G. Peeters *et al.,* Comput. Phys. Commun. **180** 2650 (2009).
[10] E. Narita *et al.,* Plasma Phys. Controlled Fusion **60** 025027 (2018).
[11] N. Hayashi and JT-60 Team, Phys. Plasmas **17** 056112 (2010).
[12] E. Narita *et al.,* Plasma Phys. Controlled Fusion **60** 025027 (2018).
[13] M.N. Rosenbluth and F.K. Hinton, Phys. Rev. Lett. **80** 724 (1998).

Spatio-temporal analysis of plasma turbulence in PANTA by using singular value decomposition

R. Takahashi [1], M. Sasaki[1,2,3]

[1] College of Industrial Technology, Nihon University
[2] Research Institute for Applied Mechanics, Kyushu University, 816-8580, Japan
[3] Research Center for Plasma Turbulence, Kyushu University, 816-8580, Japan

1 Introduction

In turbulent transport in magnetic confined plasmas, turbulence is excited by temperature and density gradients, and the excited turbulence causes transport and affects the temperature and density gradients. In addition, turbulence forms structures such as flow and rotation, and the formation of these structures suppresses the turbulence, which is a dynamic competitive state that needs to be understood. The conventional analysis method, Fourier transform, uses trigonometric functions as basis functions, which is effective for linear data, but difficult to characterize time-varying data due to its large degree of freedom. In this study, singular value decomposition was used to analyze magnetic confinement plasma data, which is suitable for extracting features with small degrees of freedom because the optimal basis can be obtained.

2 Model

Singular value decomposition of 64 channels of spatio-temporal plasma turbulence data during 0.2[s] acquired by the linearly magnetized plasma system PANTA has been analyzed using a computer. The resulting data are further analyzed.

3 Results

In Fig. 1, the vertical axis shows the spatial structure and the horizontal axis shows the time. Since the spatial data is invariant in 32ch, the vertical axis shows the combination of Modes decomposed by SVD. The last column of each magnetic field is the singular value Σ of the characteristic mode multiplied by the right singular vector Vt. In the case of 600G, the zonal flow seen in the Mode with small contribution seems to affect the Mode

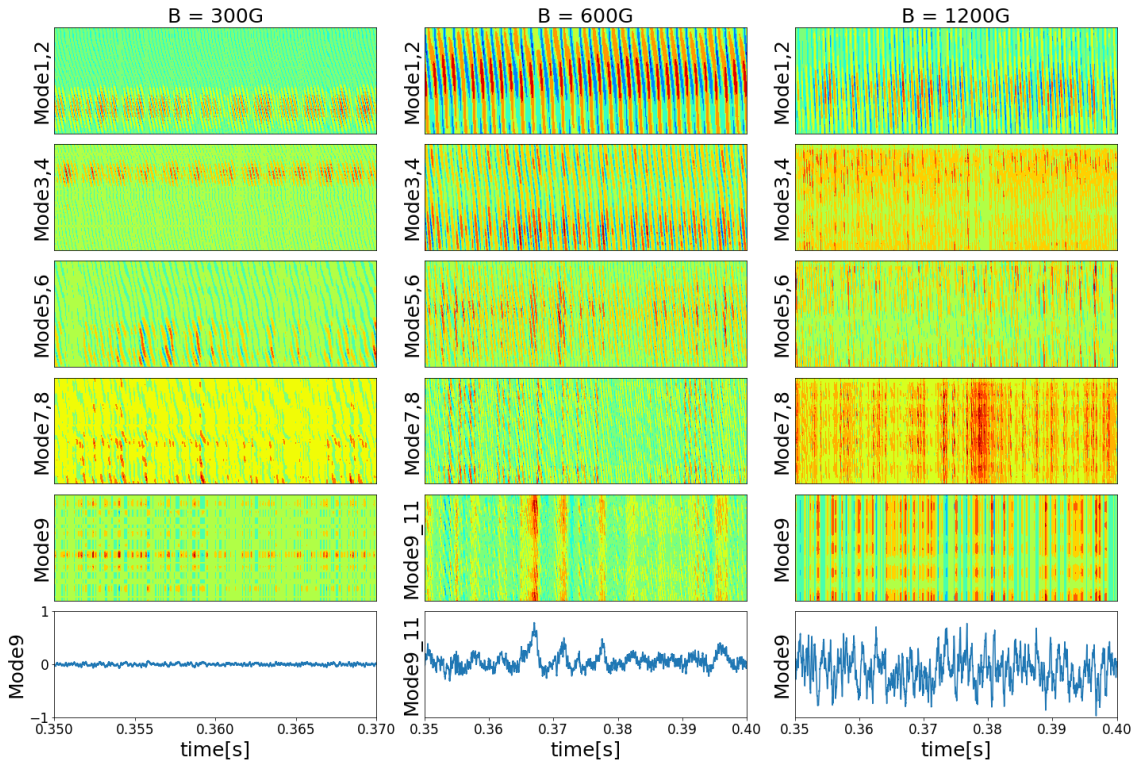

Fig.1　Results of SVD

with large contribution. On the other hand, at a magnetic field of 1200G, zonal flow-like phenomena are observed, but there is little effect on the Mode with high contribution. The reason for this is that in the 600G case, there are low-periodic areas of high intensity, while in the 1200G case, there are areas of low intensity. It was thought that because of the presence of high periodic intensity areas, the next change would occur before it could affect the high contribution Mode, and thus the effect would not be felt.

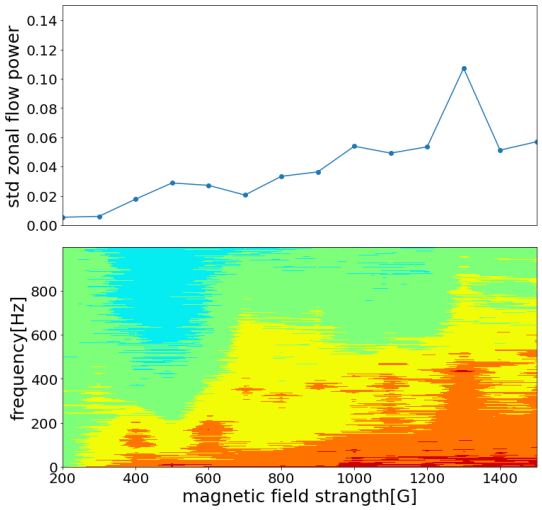

Fig.2 Frequency of zonal flow _ like

Fig. 2 shows the standard deviation (top) and frequency (bottom) of the zonal flow-like structures, which increase with higher magnetic fields, and may be related to the hypothesis.

Effect of impurities on improved confinement in tokamak discharges

Sho Nonaka[1], Naohiro Kasuya[1,2], Atsushi Fukuyama[3],
Shota Mochinaga[1], Masatoshi Yagi[4]
IGSES, Kyushu Univ.[1], RIAM, Kyushu Univ.[2], Kyoto Univ.[3], QST.[4]

1 Introduction

Presently, International Thermonuclear Experimental Reactor (ITER) is under construction. For realizing the fusion reactor, achievement of high performance plasma discharge is necessary. High confinement discharges have been obtained, which are called high β_p mode [1], reversed shear mode [2], and so on, with formation of internal transport barrier (ITB). On the other hand, high Z impurities degrade plasma performance, as tungsten planned to be used for the divertor plate of ITER. In this research, the effect of tungsten impurity is investigated in the reversed shear mode by using integrated transport simulation code TASK [3]. Dependence on impurity influx is evaluated for the heating power threshold and internal transport barrier performance.

2 Analysis

2.1 L-mode discharge

For the simulation of L-mode discharge, additional RF heating is applied at t = 1.0s, which is assumed to be equally absorbed by electrons and ions. Tungsten impurity comes from the surface of the plasma with influx $\Gamma_{in,W}$ to give a peaked profile of line radiation, which affects to form a hollow temperature profile in t = 1.5 - 3.0s as in Fig.1. On the other hand, the effect of the impurity is small in the steady state, due to reduction of impurity accumulation by RF heating. The density profile of the impurity depends on used turbulent diffusion models. Increase of the temperature which caused by RF heating leads to increase the turbulent diffusion coefficient (Fig.2).

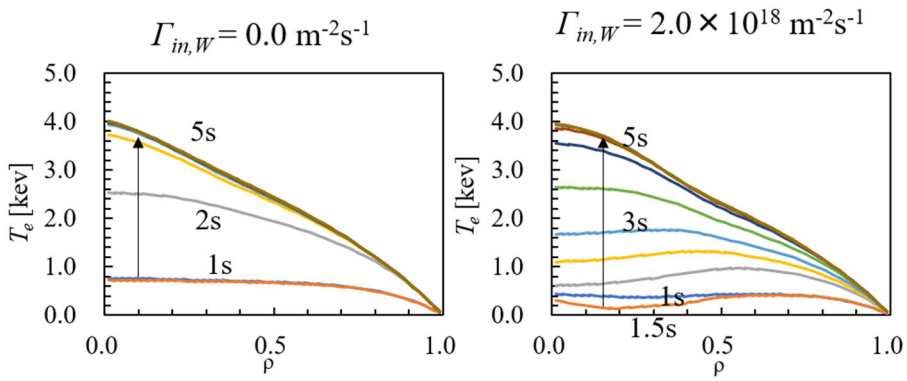

Fig.1 Temperature profile in the case of $\Gamma_{W,in}$=0.0m^{-2}s^{-1} and $\Gamma_{W,in}$=2.0×10^{18} m^{-2}s^{-1}

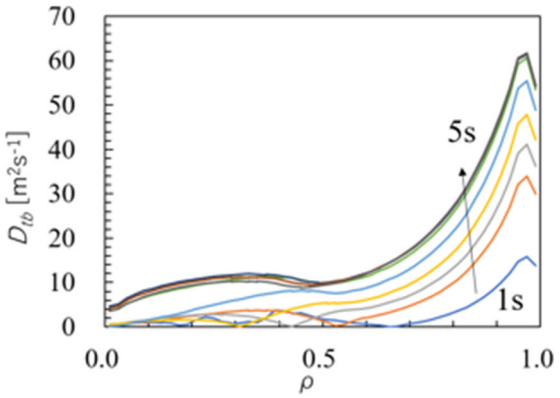

Fig.2 Radial profile of the turbulent diffusion coefficient.

2.2 Reversed shear mode discharge

For the simulation of reversed shear mode, additional RF heating is applied as the same way as the L-mode discharge, and the plasma current is increased from t = 1.0s to 2.0s in addition. In this simulation, the obtained density profile of the impurity is rather flat as in Fig.3, due to large turbulent diffusion coefficient as in Fig.4.

Dependence of the temperature on RF heating power is investigated. When the impurity influx is $\Gamma_{W,in} = 1.0\times10^{18}$ m^{-2}s^{-1}, the electron temperature is largely changed between P_{RF} = 2MW and 3MW (Fig.5). With P_{RF} = 2MW, the temperature at the center decreased after t = 2.0s and the profile becomes hollow, while the plasma is sustained with P_{RF} 3MW. The difference between two discharges is understood by comparison between the RF heating and line radiation powers. In the case when the RF heating is greater than the line radiation, large temperature plasma can be sustained.

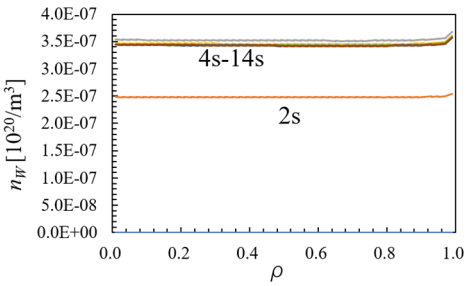

Fig.3 Density profile of the impurity

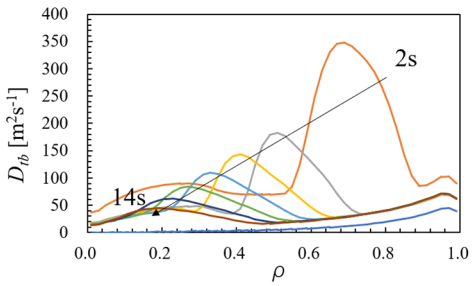

Fig.4 Radial profile of turbulent diffusion coefficient

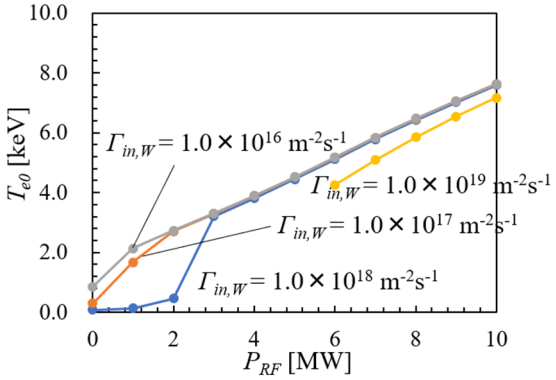

Fig.5 Dependence on the heating power of electron temperature at the plasma center.

2.3 Comparison of L-mode and reversed shear

The L-mode described in Sec. 2.1 is compared with the reversed shear mode on the condition when the RF heating is 10MW, the impurity flux is 2.0×10^{18} m^{-2}s^{-1}, the plasma current is 3MA. The effect of the impurity is small both in the L-mode and the reversed shear mode with rather large input power. In the case of the reversed shear mode, the turbulent diffusion coefficient is greater than that in the L-mode due to the larger temperature and its gradient inside of the ITB. The line radiation of the reversed shear mode is smaller than that of the L-mode, because the impurity density is reduced by the larger turbulent diffusion. The turbulent diffusion coefficients in this simulation comes from the used turbulent model; mBgB model. Another model gives the other results [4].

3 Conclusion

The effect of tungsten impurity is investigated in the reversed shear mode by using integrated transport simulation code TASK. In the L-mode discharge, peaking of line radiation by impurities affects the temperature profile in the transient phase. On the other hand, the effect of impurities is small in the steady state, because impurity density and its radiation are reduced by RF heating. In the reversed shear mode, dependence of the temperature on RF heating power is investigated with impurity influx. The case when the RF heating power is smaller than the line radiation by impurities, a high temperature plasma is not sustained. The line radiation in the reversed shear is smaller than that in the L-mode, because impurity density is reduced by lager turbulent diffusion due to ITB formation. The simulation result depends on turbulence model.

References

[1] Y. Koide, *et al.*, Phys. Rev. Lett. **72**, 3662 (1994)

[2] T. Fujita, *et al.*, Phys. Rev. Lett. **78**, 2377 (1997)

[3] M. Honda, *et al*., Nucl. Fusion **46**, 580 (2006)

[4] Erba, *et al*., Nuclear Fusion **38**, 1013 (1998)

円筒プラズマにおけるイオン質量数とドリフト波乱流構造

Drift wave turbulent structure depending on ion mass number in cylindrical plasmas

N. Kasuya[1,2], Y. Imahashi[2], H. Todoroki[2], M. Ishida[2] and M. Yagi[3]
[1] RIAM, Kyushu University, Kasuga, Fukuoka 816-8580, Japan
[2] IGSES, Kyushu University, Kasuga, Fukuoka 816-8580, Japan
[3] QST, Obuchi, Rokkasho, Aomori 039-3212, Japan
E-mail: kasuya@riam.kyushu-u.ac.jp

Variation of ion species in discharges affects performance of plasma confinement. Basic experimental devices with cylindrical configuration are used to investigate fundamental mechanism of plasma turbulence, such as formation mechanism of turbulence structures [1] and nonlinear interaction between plasma instabilities [2]. Effects of ion species have been also studied in the basic plasmas [3]. In simulations, variations of characteristic mode numbers and formed structures in plasma turbulence are predicted between different discharge gases [4]. Nonlinear simulations for PANTA linear device [5] using turbulence code NLD [6] have shown that a large number of modes with larger axial mode numbers become unstable in the case of smaller mass ions, and their nonlinear couplings gives difference in formed turbulent structures. Figure 1 shows comparison of snapshot of turbulent states in argon and helium plasmas. There are preferable azimuthal and axial mode numbers corresponding to the ion mass number.

For the calculation of resistive drift wave instability in cylindrical plasmas with homogeneous magnetic fields in the axial direction, the following set of three-field reduced fluid equations is used [8]. The time and distance are normalized by the ion cyclotron frequency Ω_{ci} and the effective Larmor radius $\rho_s = \sqrt{MT_e/eB}$ evaluated by using the electron temperature T_e, respectively. Neutral particles exist even in the center of this rather low temperature plasma, so the effect of neutrals is included by the ion-neutral collision ν_{in} terms. In addition, only charge number Z = +1 ions are considered with this range of the temperature. Dependence of the linear growthrate is obtained numerically as in Fig. 2. The simulation parameters are the followings; magnetic field B = 0.1 T, electron temperature T_e = 3 eV, plasma radius a = 7 cm, device axial length λ = 4 m, electron-ion collision frequency ν_{ei}/Ω_{ci} = 300, electron-neutral collision frequency ν_{en}/Ω_{ci} = 10, viscosities $\mu_W = \mu_V = 10^{-4}$, $\mu_N = 10^{-2}$ and $L_n = a / 5$. There are several (m, n) modes, which have positive growthrate (unstable modes) with a certain ν_{in} and A, and among them the mode with maximum growthrate is picked up, which has mode number (m_p, n_p). Here, m and n are azimuthal and axial mode numbers, respectively. Larger ν_{in} makes modes stable, and heavier ion makes m_p and n_p smaller. (m_p, n_p) = (15, 11) mode is the most unstable with helium plasma, though (3, 1) mode is with argon plasma, when ν_{in} = 0.04.

Linearization and simplification with $\phi_0 = \partial\phi_0/\partial r = V_0 = \partial V_0/\partial r = 0$ give an eigen-equation

$$\omega^2 + \left[i\nu_{in} + iP\frac{T+1}{T} \right]\omega - P\left(\nu_{in} + \frac{i\omega_*}{T} \right) = 0, \qquad (1)$$

where $P = M_i k_z^2/\nu_e$ is related to axial wave number k_z, $\omega_* = k_\theta L_n^{-1}$ is the diamagnetic

frequency, $M_i = Am_u/m_e$ is the ion mass ratio, A is the ion mass number, m_u is the atomic mass constant, $L_n^{-1} = -dN_0/dr$ is inverse of the density gradient length, and $T = k_\perp^2 + ik_r L_n^{-1}$. Here viscosities are put to be zero $\mu_W = \mu_V = \mu_N = 0$ for simplicity. The solution of Eq. (1) is

$$\omega = \frac{-i\nu_{in} - iP\dfrac{T+1}{T} \pm \sqrt{-\nu_{in}^2 + 2P\left(\dfrac{T-1}{T}\nu_{in} + 2i\dfrac{\omega_*}{T}\right) - P^2\left(\dfrac{T+1}{T}\right)^2}}{2}. \qquad (2)$$

In these parameters, ν_{in} and P have the same order of magnitude, so the expression is little bit complex. To evaluate the most unstable k_z, an analytical expression with $\nu_{in} << P << 1$ is obtained as

$$\omega \sim -iP\frac{T+1}{2T} + \sqrt{iP\frac{\omega_*}{T}}. \qquad (3)$$

Solution (3) has the maximum growthrate

$$\mathrm{Im}\,\omega = \frac{1}{4}\frac{k_\theta L_n^{-1}}{1+k_\perp^2}, \qquad \text{when} \quad P = \frac{1}{2}\frac{k_\perp^2}{\left(1+k_\perp^2\right)^2}k_\theta L_n^{-1}. \qquad (4)$$

Then, $k_\theta^2 = 1 + k_r^2$ gives the maximum of Eq. (8) with

$$\mathrm{Im}\,\omega = \frac{1}{8}\frac{L_n^{-1}}{\left(1+k_r^2\right)^{3/2}}, \text{ when } \quad P = \frac{1}{8}\frac{1+2k_r^2}{\left(1+k_r^2\right)^{3/2}}L_n^{-1}. \qquad (5)$$

For the radial direction, smaller k_r makes the mode unstable ($k_r \to 0$), and the value is determined by the boundary condition, when the global mode structure is considered. From these expression, dependence of a spectrum peak on the ion mass M_i is given to be

$$m_p \propto A^{-1/2} \quad \text{from } k_\theta \sim 1 \qquad (6)$$

and

$$n_p \propto A^{-3/4} \quad \text{from} \quad \frac{M_i k_z^2}{\nu_e} \sim \frac{1}{8}L_n^{-1}, \qquad (7)$$

considering the normalization with ρ_s. In this way, preferable k_θ and k_z are obtained, which makes the plasma most unstable. Perpendicular and parallel flow balance and delay of the response by collision is the cause of the resistive drift wave instability. In the balance, competition of the convective derivative term and the perpendicular drift (especially polarization drift) term is the key to determine the wave number spectrum.

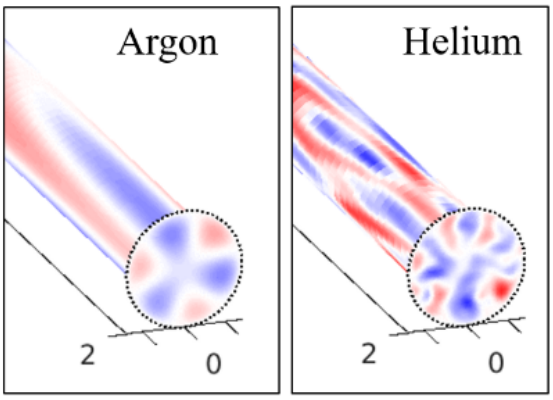

Fig.1 Numerical simulations of potential perturbations in the saturated states of plasma turbulence in cylindrical plasmas. Comparison between argon and helium discharges are shown.

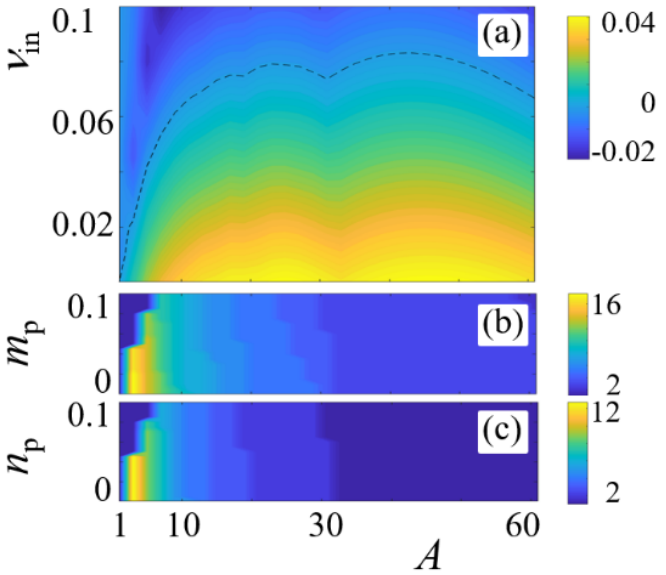

Fig.2 (a) Dependence of the maximum linear growthrate on ion mass number A and collision frequency ν_{in}. The dashed line shows the unstable boundary where the growthrate is zero. The maxima are given with different (b) azimuthal m_p and (c) axial n_p, depending on the parameters.

Acknowledgements

Authors acknowledge discussion with Dr. M. Sasaki. This study is partially supported by the Grant-in-Aid for Scientific Research (JP17H06089, JP20K03905) of JSPS, the collaboration program of NIFS (NIFS19KNST144) and of RIAM of Kyushu University.

References

[1] T. Yamada *et al.*, Nature Phys. **4**, 721 (2008).
[2] H. Arakawa *et al.*, Plasma Phys. Control. Fusion **53**, 115009 (2011).
[3] T. Kobayashi *et al.*, Phys. Plasmas **27**, 062309 (2020).
[4] S. Tomimatsu *et al.*, Plasma Fusion Res. **15**, 1403052 (2020).
[5] S. Inagaki *et al.*, Sci. Reps. **6**, 22189 (2016).
[6] N. Kasuya *et al.*, J. Phys. Soc. Jpn. **76**, 044501 (2007).